Tampere University

Jin Gong

WHITE MATTER HYPERINTENSITY AND MULTI-REGION BRAIN MRI SEGMENTATION USING CONVOLUTIONAL NEURAL NETWORK

Faculty of Information Technology and Communication Sciences (ITC)
Master's thesis
April 2020

Abstract

Jin Gong: WHITE MATTER HYPERINTENSITY AND MULTI-REGION BRAIN MRI SEGMENTATION USING CONVOLUTIONAL NEURAL NETWORK
Master's thesis
Tampere University
Master's Degree Programme in Computational Big Data Analytics
April 2020

Accurate segmentation of WMH (white matter hyperintensity) from the magnetic resonance image is a prerequisite for many precise medical procedures, especially for the diagnosis of vascular dementia. Brain segmentation has important research significance and clinical application prospects especially for early detection of Alzheimer's disease. In order to effectively perform accurate segmentation according to the MRI characteristics of different regions of the brain, this thesis proposed an optimized 3D u-net and used WHM segmentation as a pre-experiment to select the good hyperparameters (i.e. network depth, image fusion method, and the implementation of loss function) to construct an image feature learning network with both long and short skip connections. Soft voting is used as the postprocessing procedure. Our model is evaluated by a 10-fold cross validation and achieved a dice score of 0.78 for binary segmentation (WMH segmentation) and accuracy of 0.96 for multi-class segmentation (139 regions brain segmentation), outperforming other methods.

Keywords: 3D Image Segmentation, Magnetic Resonance Imaging, Brain Regions, Convolutional Neural Networks.

Contents

1 Introduction 1

2 Related Work 3

2.1 Traditional segmentation method for grayscale pictures 3

2.2 Deep learning-based segmentation method for general pictures 4

2.3 Deep learning-based segmentation method for medical images 5

3 Background 7

3.1 Basics of MRI 7

3.2 Basics of neural networks 8

3.2.1 The artificial neural networks 8

3.2.2 The back propagation 9

3.2.3 The activation function 10

3.2.4 The loss function 11

3.2.5 The optimizer 13

3.3 Basics of Convolutional neural network 13

3.3.1 The convolutional layer 14

3.3.2 The downsampling layer 16

3.3.3 The upsampling layer 17

3.3.4 The normalization layer 18

3.4 The ResNet and U-net 19

3.4.1 The ResNet 20

3.4.2 The U-net 21

3.4.3 The 3D-U-Net and V-net 22

4 Data 24

4.1 The binary segmentation 24

4.2 The multi-region segmentation 25

5 Method 30

5.1 Preprocessing 30

5.2 Model selection and training 32

5.2.1 The binary segmentation 32

5.2.2 The multi-region segmentation 35

5.3 Post-processing 37

6 Results 40

6.1 The binary segmentation 40

6.2 The multi-region segmentation 45

7 Discussion 54
8 Conclusion 57
References 62
APPENDIX 63
1 Glossary 63

1 Introduction

Magnetic resonance imaging (MRI) is a medical imaging technique used in radiology to form images of the anatomy and the physiological processes of the body (McRobbie et al. 2017). An outstanding feature of MRI imaging is that it has various imaging sequences (e.g. T1, FLAIR). In T1-weighted images, there is a high signal for fat and a low signal for water, but in T2-weighted images there is a low signal for fat and a high signal for water. Faced to a variety of MRI images, the traditional method is that the physician analyzes the images through rich experience and professional knowledge. However, for different physicians, and even for the same physician in different periods of time, the division and measurement of segmentations in the same image will be different, it makes manual segmentation subjective. Moreover, manual segmentation is time consuming. If physicians can evaluate the images with the help of specialized software, it will be conducive to a more accurate diagnosis and treatment of patients.

In recent years, a large number of image segmentation methods have emerged, including traditional segmentation methods and machine learning-based segmentation methods. Traditional segmentation methods like threshold-based segmentation (Kurita, Otsu, and Abdelmalek 1992) and edge detection-based segmentation (Xie and Tu 2015) are fast but sensitive to noise. Machine learning-based segmentation methods like VGGNet (Simonyan and Zisserman 2014) is highly depend on the depth of the network as well as the size and quality of training data. The fully convolutional network (Long, Shelhamer, and Darrell 2015) is able to do pixel-wise semantic segmentation but the results obtained are fuzzy and smooth due to upsampling, and are not sensitive to details in the image. Until now, the algorithm widely used in the field of medical image segmentation is still the u-net (Ronneberger, Fischer, and Brox 2015) proposed in 2015, and its variants.

The reason why MRI segmentation is a challenging problem is that its images have unique properties. First, MRI images are three-dimensional images and have spatial features. If the 3D image is sliced in a certain dimension and then the ordinary 2D segmentation method is applied, a lot of useful information will be lost. This thesis will prove it later in Chapter 5. Therefore, it is necessary to choose an appropriate 3D segmentation method. Another problem is the size of training data. Once the structure of the network is determined, the generalization ability depends on whether there is sufficient training set. If only one or two specific regions or lesions are needed, usually they can be labelled manually by medical experts. Furthermore, the original MRI usually has 1 channel only which means it is a gray scale image, by combining different sequences, more channels can be added. Portrait

or landscape shots with a mobile phone or camera have at least 3 channels. The images with RGB channels carry more information than gray scale images. Due to hardware and technology limitations, the resolution of medical images is relatively low. The final problem is the robustness and precision. Behind each medical image there is a patient, and incorrect segmentation might lead to wrong diagnoses and unsuitable treatment plans. In particular, brain segmentation requires an extremely high accuracy. These reasons make brain segmentation difficult but also meaningful.

In this thesis, several experiments are performed to evaluate the performance of the existing popular networks. Based on the results of these experiments, an optimized 3D-U-net is developed in this thesis. It is applicable to extreme multiple classes segmentation and extreme small area segmentation. It uses residual units, which add the identity mapping of the input to the current convolutional layer, to enhance the learning ability of the network. The distribution of weights is considered in the design of each layer of the neural network, thereby enhancing the generalization ability of the model. Meanwhile, to do patch merging in post-processing procedure, a new soft-vote based on probability is designed and tested as effective to increase the overall accuracy.

This thesis is structured as follows. Chapter 2 discusses briefly the general image segmentation methods, popular medical segmentation methods and their pros, cons and applications. Chapter 3 introduces the key theory behind the applied method (i.e. the basics of 2D and 3D U-net, V-net ,loss and activation functions). Chapter 4 focus on the data used in the experiments. In Chapter 5, a detailed algorithm from pre-processing to training and post-processing is explained. A comparison between the performance of the other models and the modified model introduced in this thesis is shown in Chapter 6. Chapter 7 and Chapter 8 discusses the limitations of the work and points out the potential directions of the future work and provides conclusions. The appendix contains the glossary of the thesis.

2 Related Work

In this chapter, a review of previous research works related to brain MRI segmentation is presented.

2.1 Traditional segmentation method for grayscale pictures

In this part, we will introduce the methods that were used to perform image segmentation using digital image processing, topology, and mathematics before deep learning became popular. Of course, with the increase of computing power and the continuous development of deep learning, some traditional segmentation methods can no longer be compared with deep learning-based segmentation methods, but some genius ideas are still very worthwhile for us to learn.

The simplest method is the threshold-based segmentation (Kurita, Otsu, and Abdelmalek 1992). The basic idea of the threshold method is to choose one or more gray-scale values as thresholds based on the gray-scale characteristics of the image, to compare the gray-scale value of each pixel in the image with the thresholds, and finally to segment the image according to the classes that the pixels belong to. Therefore, the selection of the thresholds influences the result a lot. The threshold method is particularly suitable for the images that the gray-scale values in different regions are significantly different. Therefore this fast method is very sensitive to noise and is not robust.

The region-based segmentation (Chang and X. Li 1994) method is a segmentation technique takes spacial information into concern. There are two basic forms of region-based extraction methods with different directions: one is region growth, which starts from one pixel and gradually merges its neighbour areas which belong to the same region to the pixel; the other starts from the whole image and gradually cuts the pixels that do not belongs to the target region. Watershed algorithm (Parvati, Rao, and Mariya Das 2008) has similarities with it. These algorithms can be seen as unsupervised or semi-supervised algorithms. This type of algorithm is ideal for segmentation of complex scenes defined by some complex objects, or for segmentation of certain natural scenes, and other similar images which lack sufficient prior knowledge.

Generally, the gray-scale value of pixels on the boundaries of different regions changes drastically. If a picture is transformed from the spatial domain to the frequency domain by Fourier transform, the edges correspond to high-frequency parts. This is a very simple edge detection algorithm and the segmentation method based on this algorithm is so called edge-based segmentation method. The sim-

plest edge detection method is the parallel differential operator method (Bevington and Mersereau 1987), which uses the nature of discontinuous pixel values in adjacent regions and uses first-order or second-order derivatives to detect edge points. Therefore, methods based on surface fitting (Monga and Benayoun 1995), methods based on boundary curve fitting (Kolomenkin, Shimshoni, and Tal 2009), methods based on reaction-diffusion equations (Nomura et al. 2011)) and methods based on deformation models (Wu and Yu 2004) have also been proposed. Edge detection cannot guarantee edge continuity and closure. Image segmentation method based on wavelet analysis and wavelet transform (J. Li 2003) can solve this problem. With the help of Hilbert transform (Dibal et al. 2018), a better result is shown.

Nowadays the most widely used traditional method in medical area is atlas-based segmentation. Atlas is a fully labeled database, for instance, the atlas of BrainWeb (Cocosco et al. 1997) contains various brain structures in CT images labeled by doctors. The earliest atlas-based segmentation was based on nonrigid registration, which registered the test image with the data in atlas, and then used the label propagation method to transfer the labels in the atlas to the test image through the registration mapping, thereby completing the segment tasks. Obviously, the atlas-based segmentation method is highly dependent on the accuracy of nonrigid registration with high computational complexity.

2.2 Deep learning-based segmentation method for general pictures

As mentioned above, VGGNet (Simonyan and Zisserman 2014) is an example of feature encoder based segmentation method. By repeatedly stacking layers with 3 $\times$ 3 small convolution kernels and 2 $\times$ 2 maximum pooling layers, it extract image features. It builds convolutional neural network as deep as 16 to 19 layers and finds that deep networks have better performance comparing to the shallow ones. VGGNet won the runner-up of the ILSVRC 2014 competition and the champion of the positioning project. VGGNet occupies a lot of memory due to the large number of layers and the many parameters of the last three fully connected layers.

Although new models with better performance appear every year, the improvement to previous work is not so obvious. One of the important problems is that deep learning networks are stacked. At a certain depth, the gradient disappears, which causes the error increase effect to become worse. The gradient cannot be fed back to the previous network layer during backward propagation, which makes it difficult to update the parameters of the previous network layer and the training effect becomes worse. At this time ResNet (He et al. 2016) stood out and became an important turning point in the development process of deep learning. The core idea of ResNet

is to introduce identity mapping in the network, which directly transmitted the input information to the subsequent layers. During the learning process, only the residuals of the previous network output can be learned. The detailed algorithm of Resnet will be introduced in Chapter 3.

The convolutional neural network will lose some detailed information when sampling, so the purpose is to get more characteristic value. However, this process is irreversible, and sometimes the resolution of the image is too low, and details are lost during subsequent operations. Therefore, we can complete some missing information through upsampling to obtain a more accurate segmentation boundary. The most famous model in this area is the fully convolutional network (Long, Shelhamer, and Darrell 2015) so called 'FCN'. In the deconvolution-upsampling structure in FCN, the picture is first up-sampled (enlarged pixels); then convolved (weights are obtained through learning). FCN has become an industry benchmark in the field of image segmentation. Most of the segmentation methods will use FCN or part of it more or less.

2.3 Deep learning-based segmentation method for medical images

DeepMedic (Kamnitsas, Ledig, et al. 2017) is a 3D multi-scale CNN with two parallel paths. The upper path extracts small area features, and then performs residual block convolution and downsampling. The lower path extracts large area features. Such a dual architecture can ensure that good detail information (local information) can be extracted in the normal resolution channel, and good high-level information (relatively large range information) can be maintained in the low resolution channel. Therefore, the segmentation information and positioning information are accurate. It is wildly used to segment brain tumors (Kamnitsas, Bai, et al. 2017).

Another method called U-net (Ronneberger, Fischer, and Brox 2015) is also widely used in the area of medical images segmentation. The original U-net is made for 2D images of cells. It is very similar to the FCN mentioned before. In the encoding part, a new scale is constructed each time it passes through a pooling layer, repeated for 5 times. The decoding part is fused at the same scale as the number of channels corresponding to the feature extraction part each time it is sampled. In this way, richer context information is obtained. In the process of decoding, detailed information is enriched through multi-scale fusion, and the accuracy of segmentation is improved. Afterwards, the same authors proposed a 3D U-net (Çiçek et al. 2016) and another group of researchers proposed the V-net (Milletari, Navab, and Ahmadi 2016) with the similar idea. They separately segmented the kidney of xenopus and the prostate volume in MRI, and achieved good results. However, only a very limited

number of multi-class segmentation can be done by these methods by doing binary segmentation several times.

With the great success of deep learning in the field of computer vision, the image semantic segmentation method based on convolutional neural networks has made breakthrough progress, taking image segmentation to a new height. How to continue to improve the accuracy of the segmentation algorithm and reduce the complexity of the segmentation algorithm are issues worthy of further research. Consequently, a better multi-class (over 100 classes) segmentation method for 3D medical images is needed.

3 Background

This part of the thesis introduces some basic knowledge of medical images, neural network and image processing. These concepts will be helpful for readers to understand the architecture of the algorithm in Chapter 5. Three networks whose ideas are used in the algorithm in Chapter 5 are analyzed here as well.

3.1 Basics of MRI

Medical imaging has a variety of image modalities, such as MRI, computed tomography (CT), positron emission tomography (PET), ultrasound imaging, and so on. Imaging can obtain images that reflect the physiological and physical characteristics of the human body in two and three-dimensional areas. The content of this thesis mainly focuses on the characteristics of MR imaging. Each element in the two-dimensional image is called a pixel, and each element in the three-dimensional area is called a voxel. In some cases, the three-dimensional image can be represented as a series of two-dimensional slices for observation. The advantage is that the calculation complexity is low and requires less memory.

Magnetic resonance imaging (MRI) is the most widely used technique in the field of radiography. As a dynamic and flexible technology, MRI can achieve variable image contrast. This process is achieved by using different pulse sequences and changing imaging parameters corresponding to the longitudinal relaxation time (T1) and lateral relaxation time (T2). T1 and T2-weighted imaging signal strength is related to the characteristics of specific tissues (Shenton et al. 2001). Imaging parameters used in the dataset of this thesis is listed as Table 3.1. The 3D images used in this study are rebuilt from a number of 2D slices in the axial direction.

Table 3.1 *Imaging parameters of the dataset.*

Parameters	**FLAIR**	**T1**
Echo time	100-140 ms	4-7 ms
Repetition time	6000-10000 ms	10-25 ms
Inversion time	2000-2400 ms	
Flip angle		$15^\circ - 30^\circ$
Voxel size	$0.4 - 1 \times 0.4 - 1 \times 5 - 7.5mm^3$	$0.5 - 1 \times 0.5 - 1 \times 1 - 1.5mm^3$
Number of slices	15-38	256

MRI has a good imaging ability for soft tissues, very high resolution, and a high signal-to-noise ratio. Different pulse sequences can be used to obtain multi-channel images with varying contrasts, which can be used for target segmentation and classification of different anatomical structures (Vandenberghe and Marsden

2015). However, there are many artifacts in MRI, such as the partial volume effect, random field noise, intensity non-uniformity, gradient artefacts, motion artefacts, etc (Sharma and Aggarwal 2010). In addition, the acquisition of MRI takes a considerable time, and it is often difficult to obtain uniform image quality under normal conditions.

3.2 Basics of neural networks

Before we talk more about neural networks, let us understand some terms. Strictly speaking, the neural network to be created is called an artificial neural network (ANN), to distinguish it from the real neural network in the human brain (a network of brain cells connected). We may also see neural networks to appear under some names, such as connected machines (also known as connectionism in this field), parallel decentralized processors (PDP), thinking machines, etc., but we will use the term "neural network". It is used to refer to "artificial neural networks".

3.2.1 The artificial neural networks

A typical neural network consists of several, hundreds, or thousands of artificial neurons called "units". They are arranged in a series of layers, and each layer is connected to each other. Some of these neurons are called "input units" and are used to receive a variety of information from the outside world. Neural networks use this information to learn, recognize patterns, or perform other processing. There are also some neurons on the other side of the neural network, which are opposite to the "input unit". They show the learning status of the neural network. These neurons are called "output units". Between the "input unit" and the "output" unit there are also one or more layers composed of "hidden units", which together with the "input layer" and "output layer" form a neural network. Figure 3.1 presents an example of a four-layer simple fully connected neural network.

Fully connected means that for all the layers that is not the input layer, each neuron inside is connected to all the neurons in the preceding layer. The connection is the "weight", which can be positive (when one unit fires another) or negative (when one unit suppresses another). The higher the weight value, the greater the influence of one unit on the other unit (this is the same principle that human brain cells stimulate each other through synapses). Figure 3.2 contains an example of a perceptron in the i^{th} hidden layer. Activation computation of one neuron is represented mathematically as:

$$y = f(\sum_{j=1}^{n} w_{ij} \times x_j + b_i), \tag{3.1}$$

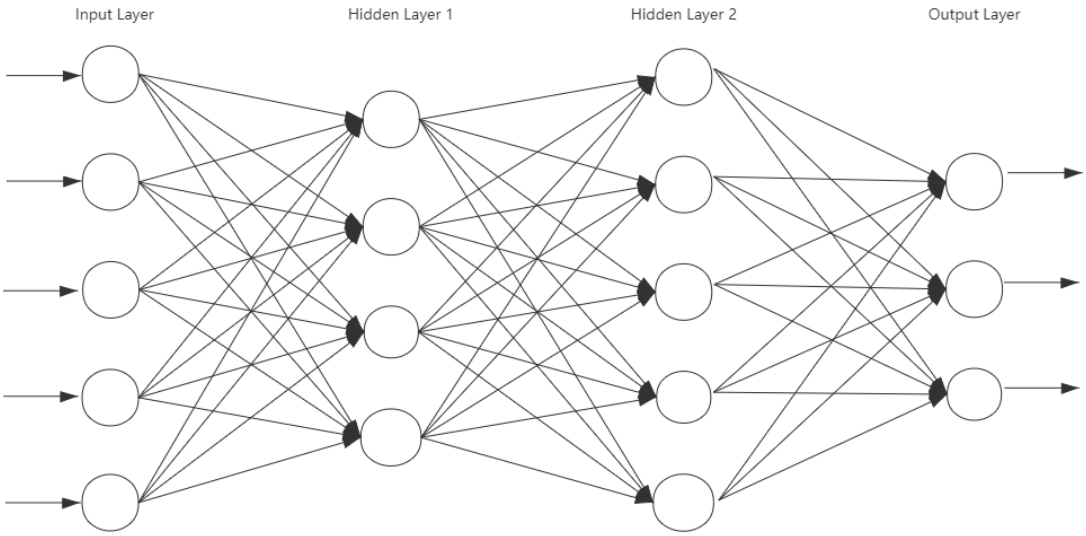

Figure 3.1 *An example of neural network with an input layer, 2 hidden layers and an output layer.*

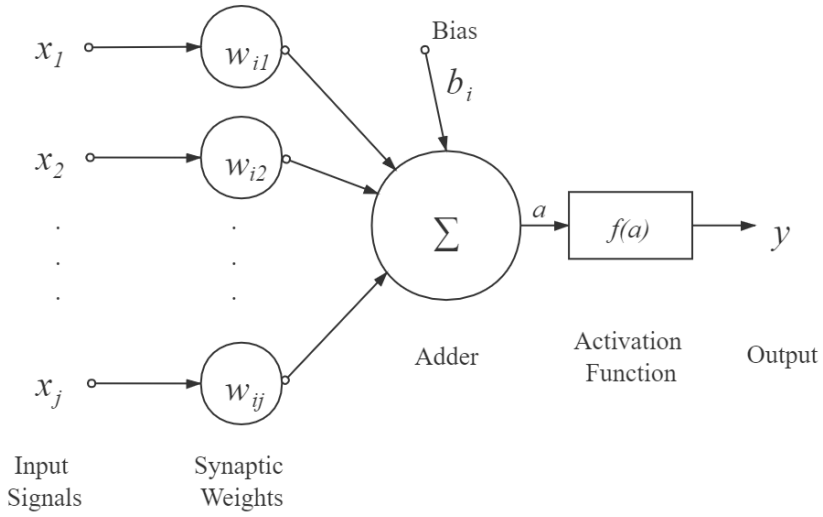

Figure 3.2 *An example of a perceptron of the i^{th} layer.*

where y is the output of this neuron, $f(x)$ is the activation function and b_i is the bias. Bias can help to improve the flexibility of neural networks. w_{ij} is the weight between the neuron before and the current neuron.

3.2.2 The back propagation

Information is moved through neural networks in two ways, forward and backward. When the neural network is in training period or predicting period, the information

travels from the input units and go through all the hidden units and finally reaches the output units. A neural network of this design is called a "feed-forward network". Not all units are always "active". Each neuron receives input from the preceding neuron except the input neurons, and the input is multiplied by the corresponding weights. In this way, each unit sums all the input information it receives and compare to a threshold. If the result is greater, the unit will become "activate" and excite the unit connected to it.

The neural network learns using a feedback mechanism called "back propagation" (Werbos 1974), which consists of both the forward propagation process and the back propagation process. In the forward propagation process, if the final output is different from the optimal value, then the sum of the square of the difference is computed and transfer to back propagation, and the partial derivative of the objective function on the weight of each neuron is found layer by layer to form the target. The ladder of the function's weight vector is used as the basis for modifying the weight. The learning of the neural network is completed in the process of modifying the weight. When the error (the sum of the square of the difference) reaches the expected small enough value, the process ends.

3.2.3 The activation function

In neural networks, there is a functional relationship between the inputs and outputs of the hidden and output layer nodes. This function is the activation function. If there is no activation function, the input and output have a linear relationship, but in reality many models are non-linear. The introduction of the activation function can increase the non-linearity of the model. The activation functions used in the network in Chapter 5 are ReLU (Bishop et al. 1995), sigmoid (Cybenko 1989) and softmax (Bishop et al. 1995).

Sigmoid function is also called Logistic function, which has a very important position in the field of machine learning. First, Sigmoid's equation is

$$Sigmoid(x) = \frac{1}{1 + e^{-x}}. \tag{3.2}$$

Its domain is $(\infty, +\infty)$ and range is $(0, 1)$. The function is continuous and smooth in the domain and has derivative everywhere (Cybenko 1989). In most cases, there is no way to know the form of the probability distribution of unknown events, and when it is not known, the normal distribution is the best choice because it is the most likely form of expression of all probability distributions. After assuming that the probability distribution of an event conforms to the law of normal distribution, to analyze its possible probability, it depends on its integral form. The format of the integral of the Sigmoid function is very similar to the normal distribution

function. Because of the simple equation and very small calculation of Sigmoid, it is selected as a substitute function. Sigmoid functions are generally used to solve binary classification problems.

When the Sigmoid function is used as the activation function and the gradient is less than 1 in the deep model, the learning ability will be attenuated layer by layer. This phenomenon is particularly obvious and will cause the model to stagnate called vanishing gradient problem (Hochreiter et al. 2001). For non-linear functions, rectified linear unit (ReLU) has no gradient disappearance problem because the gradient of the non-negative interval is constant. The equation of ReLU is shown below,

$$ReLU(x) = \max(0, x). \tag{3.3}$$

For linear functions, ReLU is more expressive, especially in deep networks. The model implemented by ReLU can better mine related features and fit the training data. In deep learning, we generally use ReLU as the activation function of intermediate hidden neurons. In AlexNet (Krizhevsky, Sutskever, and G. E. Hinton 2012) it is proposed that using ReLU to replace the traditional activation function is a major advance in deep learning.

Softmax (Bishop et al. 1995) is used in the multi-classification process. It maps the output of multiple neurons into the (0,1) interval with the function

$$Softmax(x)_i = \frac{exp(x_i)}{\sum_j exp(x_j))}. \tag{3.4}$$

Suppose we have an array, x_i representing the i-th element in the array. Then the Softmax value of this element is the exponent of the element, divided by the sum of the exponents of all elements.

3.2.4 The loss function

In the calculation of neural networks, we often need to calculate the difference between the score S_1 calculated according to the feed forward propagation of the neural network and the score S_2 calculated according to the correct labeling, and to calculate loss before applying back propagation. Loss is usually defined as cross entropy. The loss function guides the direction of model optimization.

It is very easy to calculate the cross entropy loss through out the softmax value. Cross entropy measures the difference between the true sample label and the predicted probability. For binary classification problem, the loss function called binary cross entropy is applied. For multiple classification problem, the categorical cross entropy is applied. Equation 3.5 shows the basic form of cross entropy for an array

containing n elements.

$$H(p,q) = -\sum_{i=1}^{n} p(x_i)log(q(x_i)), \tag{3.5}$$

where p is the true probability of the sample, q is the probability predicted by the model. Note that the labels in multiple classification task should be changed to one-hot vector before training. One hot coding is the process of transforming categorical variables into a form that machine learning algorithms can easily use. It uses the bit status register to encode each state. Each state has only one bit that is valid and all the other bits are 0. Figure 3.3 is an example of how to change normal sequential label to one hot label and calculate the cross entropy.

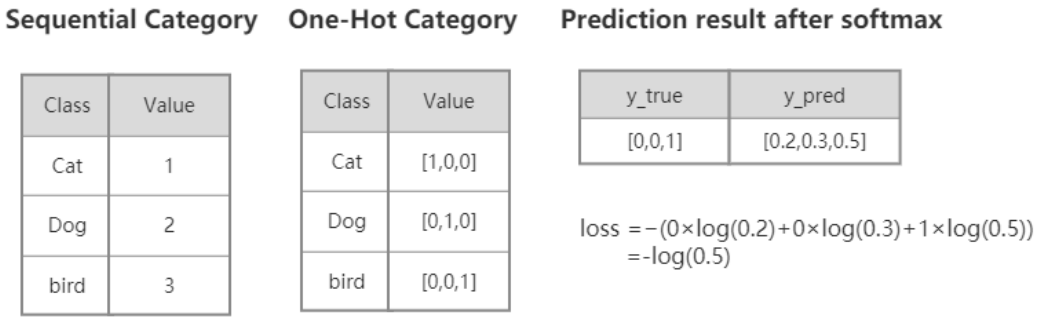

Figure 3.3 *An example of one-hot coding a 3-class case. Including the one-hot embedding and loss calculation*

The dice loss is proposed in V-net (Milletari, Navab, and Ahmadi 2016). One of the reasons is that the anatomical structure of interest only occupies a very small area of the scan, so that the learning process falls into the local minimum of the loss function. Therefore, we must increase the weight of the prospects. Dice can be understood as the degree of similarity between the two contour areas, which is defined as:

$$Dice\_score(A,B) = \frac{2 \times |A \cap B|}{|A \cup B|}, \tag{3.6}$$

where A and B are used to represent the point set contained in the two contour areas.

Dice can also be expressed as:

$$Dice\_score = \frac{2 \times TP}{2 \times TP + FP + FN}, \tag{3.7}$$

where TP, FP, and FN are the number of true positives, false positives, and

false negatives, respectively. To prevent the denominator from being zero, a Laplace smoother can be added to the dice score:

$$Dice\_score = \frac{2 \times TP + 1}{2 \times TP + FP + FN + 1}. \tag{3.8}$$

The dice loss is the opposite to dice score. Here we use $1 - dicescore$ to represent dice loss:

$$Dice\_loss = 1 - \frac{2 \times TP + 1}{2 \times TP + FP + FN + 1}. \tag{3.9}$$

3.2.5 The optimizer

Deep learning can be reduced to an optimization problem, which minimizes the objective function $J(\theta)$; in the optimization process, first the gradient $\nabla J(\theta)$ of the objective function is solved and then the parameter θ is updated to the negative gradient direction, $\theta_t = \theta_{t-1} - \eta \nabla J(\theta)$ where η is the learning rate, which indicates the step size of the gradient update. The algorithm that the optimization process depends on is called an optimizer. It can be seen that the two cores of the deep learning optimizer are the gradient and the learning rate. The former determines the direction of parameter update and the latter determines the degree of parameter update. The reason why the deep learning optimizer uses gradients is that for higher-dimensional functions, the higher-order derivative has a large computational complexity and is not practical for the optimization of deep learning. There are many types of deep learning optimizers, and research in the academic world has also been very active. Adam (Kingma and Ba 2014) is mainly used in the network proposed in this thesis.

Adam combines the advantages of two optimization algorithms, AdaGrad (Duchi, Hazan, and Singer 2011) and RMSProp (Tieleman and G. Hinton 2012). Adam is simple to implement, computationally efficient, and requires less memory comparing to AdaGrad and RMSProp. It is very suitable for large-scale data and parameter scenarios.

3.3 Basics of Convolutional neural network

Convolutional neural network (Bouvrie 2006) makes the image go through a series of convolutional layers, non-linear layers, pooling (downsampling) layers and fully connected layers, and finally get the output. Figure 3.4 represents an example of a 2D CNN with 2 convolutional layers, a maxpooling layer and 2 fully connected layers. The output can be the probability of an individual classification or a group of classifications that best describe the image content. The challenge is understanding how each of these layers works.

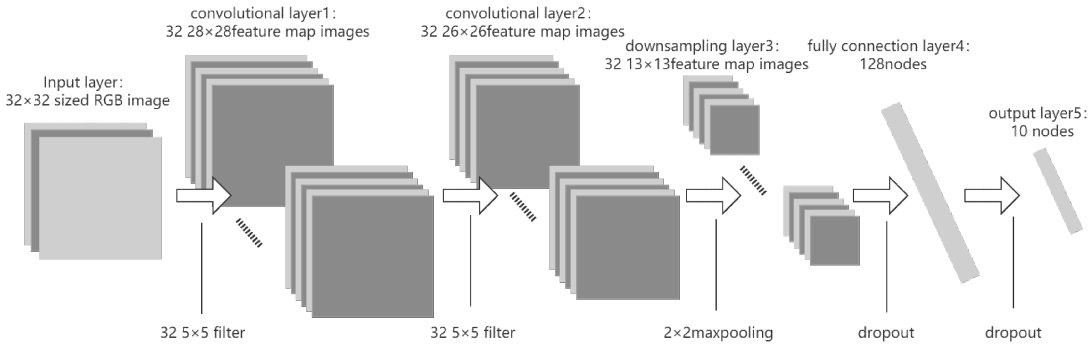

Figure 3.4 *A 2D CNN example. The input is a* 32×32 *3-channel RGB image.*

3.3.1 The convolutional layer

The first layer of a CNN is usually a convolutional layer. As the example shown in Figure 3.4 ,the input is an array of $32 \times 32 \times 3$ pixel values. Imagine that there is a 5×5 sized frame on the upper left corner of the image. In machine learning terms, this frame is called a filter (kernel), and the area inside the frame is called a receptive field. The depth of the filter must be the same as the depth of the input (to ensure that mathematical operations can be performed), under gray-scale condition the depth is 1 and under RGB condition the depth is 3, so the filter size is $5 \times 5 \times 3$. The frame can slide on the image freely and on each position it can do a convolution operation, that is, the value in the filter is multiplied(dot product) by the original pixel value in the image. The sum (sum of 75 products in this case) indicates the convolution result of the current position of the frame. The process is repeated at every position on the input. (The next step is to move the filter 1 unit to the right, then 1 unit to the right, and so on.) Each specific position on the input produces a number. After the filter slides through all the positions, we will get an array of 28 x 28 x 1, which we call activation map or feature map. The reason for a 28×28 array is that a 5×5 filter can cover 784 different positions on a 32×32 input image. These 784 positions can be mapped into a 28 x 28 array. Figure 3.5 shows an example of a 10×10 sized images and a 5×5 sized filter. Note that there is only one kernel in this example and if there are 3 kernels the output would change to 3 6×6 matrices. The more filters used, the better the spatial dimensions are preserved.

For two-dimensional convolution, the convolution kernel performs sliding window operations on the spatial dimensions of the input image (that is, (height, width) two dimensions). Each group of values in the sliding window are convolved to the value of a pixel (or a voxel in 3D cases) in the output image. The difference in Figure 3.6 between 3D and 2D convolution is that the input image has one more depth dimension and the convolution kernel has one more dimension, so the convolution

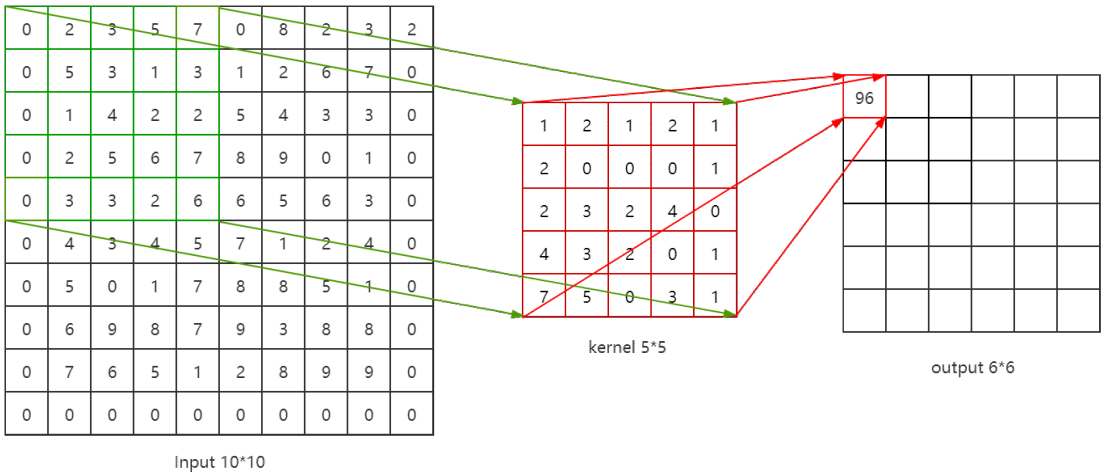

Figure 3.5 *An 2D convolutional layer example. The input is a* 10×10 *1-channel grayscale image.*

kernel performs sliding window operation on the spatial dimensions (height and width) and depth dimensions of the input 3D image. Each sliding window performs related operations with the values in the window to obtain a value in the output 3D image (see Figure 3.6(b)).

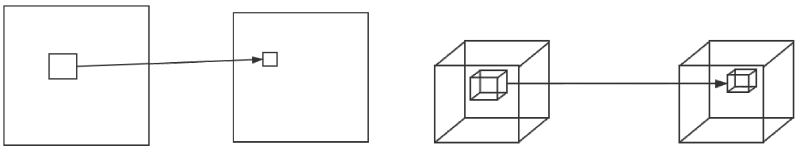

(a) 2D example. (b) 3D example.

Figure 3.6 *One channel case for both 2D and 3D convolution.*

To change the behavior of the convolutional layer, there are two main parameters that we can adjust. Padding and stride can influence the convolutional layer by changing the number of steps that the filter moves which will lead to different results.

The stride influences the number of convolution operations. In the previous example, the filter convolved the input by moving one unit at a time. The stride is the number of pixels or voxels that the filter moves at a time. In that example, the stride is set to 1 by default. The stride is usually set to ensure that the output is an integer and not a fraction. Figure 3.7 shows a 7×7 input image and a 3×3 filter (without considering the third dimension for simplicity) with strides of 1 and 2.

In the Figure 3.5, it is easily found that the output has a different size comparing to the input. The size of the image is shrinking rapidly dur to the information loss happened at the boarder area. In the early layers of the network, we wanted to

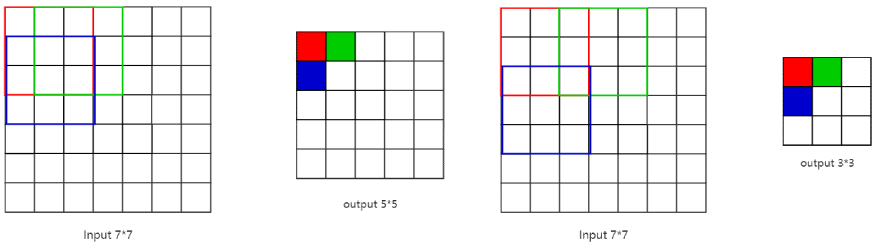

(a) The stride is 1. (b) The stride is 2.

Figure 3.7 *An example of different strides for a* 7×7 *input and a* 3×3 *kernel, the outputs are different with different strides.*

retain as much information as possible about the original input so that we could extract those low-level features. By adding zero padding of sized 2 with the same filter and stride, the size of the output can be kept as 10×10. Figure 3.8 shows an example that the output remains the same size as the input.

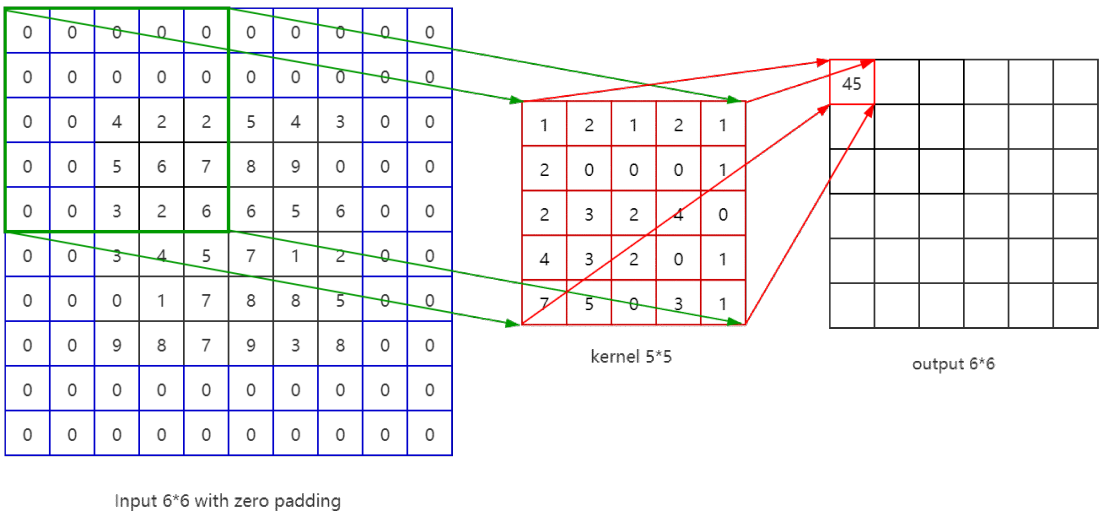

Figure 3.8 *A zero-padding example. The input is a* 6×6 *1-channel grayscale image and the output remains the same size.*

3.3.2 The downsampling layer

In Figure 3.4 there is a downsampling layer. There are also several methods to choose from in this category, the most popular of which is max-pooling. It basically uses a filter (usually 2x2) and a stride of the same length. The input image is divided in to several sub-regions and the size of each sub-region is equals to the size of the filter. Each value of a pixel or voxel in the output is the maximum

value in a sub-region. There are other options for the pooling layer, such as average pooling (M. Lin, Q. Chen, and S. Yan 2013) (see Figure 3.9) and L2-norm pooling (Carreira et al. 2012). The intuitive reasoning behind this layer is that once we know a particular feature in the original input (which will have a high activation value here), its relative position to other features is more important than its absolute position. It is conceivable that this layer greatly reduces the spatial dimension of the input volume (the length and width have changed, but the depth has not changed). This serves two main purposes. The first is that the number of weight parameters is reduced, thus reducing the computational cost. The second is that it can control overfitting. Overfitting refers to a model that matches the training sample so much that it does not produce good results when used in validation and testing groups.

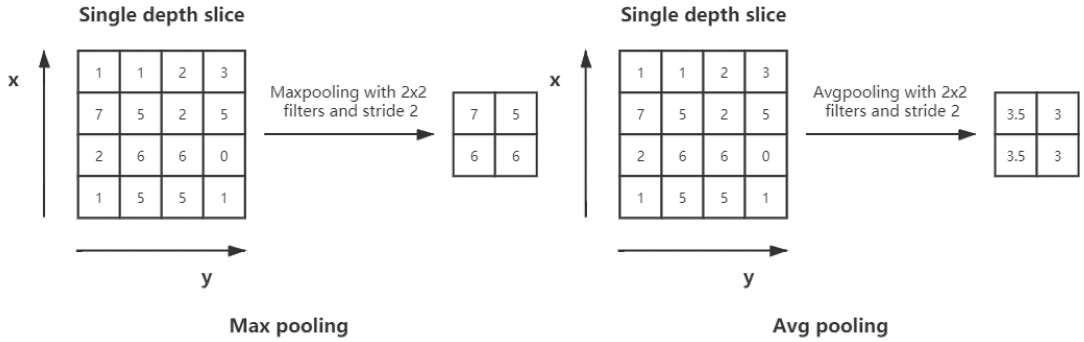

Figure 3.9 *Two downsampling examples. The left one is the max-pooling and the right one is the average-pooling.*

In Figure 3.4 there are also two dropout layers. The dropout layer (Srivastava et al. 2014) will "drop out" a random activation parameter set in this layer, that is, set these activation parameter sets to 0 in the forward pass. In a way, this mechanism forces the network to become more redundant. What this means is that the network will be able to provide a suitable classification or output for a particular sample, even if some activation parameters are discarded. This mechanism will ensure that the neural network will not "over-match" the training samples, which will help to alleviate the problem of overfitting.

3.3.3 The upsampling layer

In the field of deep learning applied in computer vision, the size of the output tends to become smaller after the features of the input image are extracted by a convolutional neural network (CNN), and sometimes we need to restore the image to its original size for further calculations (e.g. semantic segmentation of images).

Upsampling is an operation that expands the image size and to realize the mapping of the image from small resolution to large resolution.

There are three common methods for upsampling: bilinear interpolation (M. C. Seiler and F. A. Seiler 1989), Transposed Convolution (Radford, Metz, and Chintala 2015), and Unpooling (Turchenko, Chalmers, and Luczak 2017). Only the deconvolution (also called as transposed convolution) is used in this thesis. It is not a complete inverse process of forward convolution. Deconvolution is a special type of forward convolution. First, it expands the input by adding 0 according to a certain proportion, then rotates the convolution kernel, and finally performs the forward convolution. The following Figure 3.10 depicts an example of a deconvolution process.

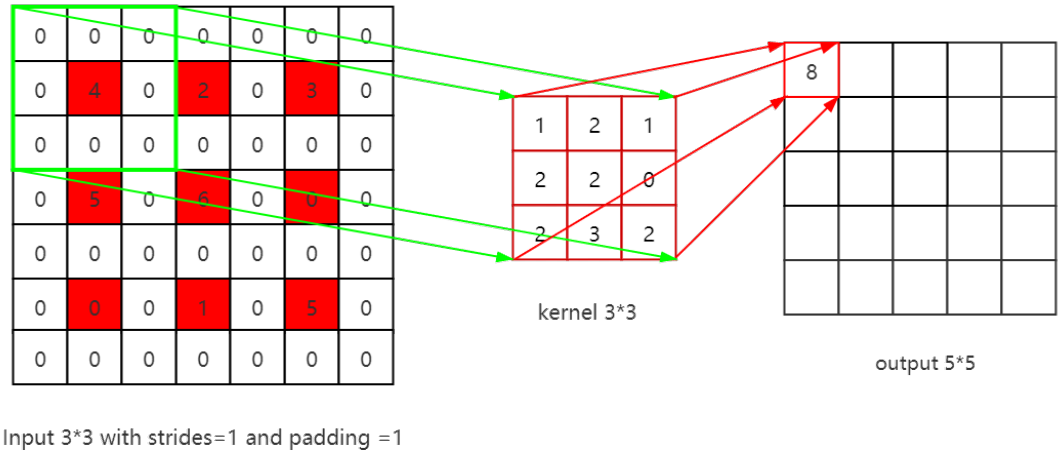

Figure 3.10 *The image size changes from* 3×3 *to* 5×5 *after deconvolution.*

3.3.4 The normalization layer

When passing the images to the neural network, the images should be normalized beforehand. Normalization is to transform the original image to be processed into a corresponding unique standard form through a series of transformations (the standard form image has invariant characteristics for affine transformations such as translation, rotation, and scaling). That is, the invariant moment of the image is used to find a set of parameters so that it can eliminate the impact of other transformation functions on the image transformation. Normalization accelerates the speed of gradient descent to find the optimal solution. The most common method is the zero-mean normalization. The processed data conforms to the standard normal distribution, that is, the mean is 0, the standard deviation is 1, and its conversion function is

$$f(x) = \frac{x - \mu}{\sigma}, \tag{3.10}$$

where μ is the mean of all pixels (voxels) and σ is the standard deviation of all data.

The method used in this thesis is the Min-max normalization. This algorithm is a linear transformation of the original data so that the result falls into the interval [0,1]. The conversion function is as follows:

$$f(x) = \frac{x - \min(X)}{\max(X) - \min(X)}, \tag{3.11}$$

where $\min(X)$ is the minimum value of all pixels (voxels) and $\max(X)$ is the maximum.

Normalization happens not only before the network, but also along the network. As the training progresses, the parameters in the network are continuously updated with gradient descent. On the one hand, when the parameters in the underlying network change slightly, these weak changes are amplified as the number of network layers deepens due to the linear transformation and non-linear activation mapping in each layer (similar to the butterfly effect). The change of parameters causes the input distribution of each layer to change, and the upper-layer network needs to constantly adapt to these distribution changes, making our model training difficult. This phenomenon is called Internal Covariate Shift (Ioffe and Szegedy 2015). Because of the internal covariate shift the network needs to be constantly adjusted to adapt to changes in the input data distribution, resulting in a decrease in the network learning speed. Meanwhile, the network training process is easy to fall into the gradient saturation region, which slows down the network convergence speed.

For each hidden layer neuron, the input distribution that gradually maps to the non-linear function and moves closer to the limit saturation zone of the value interval is forced to return to a relatively standard normal distribution with a mean of 0 and a variance of 1, so that the input value of the non-linear transformation function is in a more sensitive area to avoid the problem of gradient disappearance. This is the idea of batch normalization (Ioffe and Szegedy 2015).

3.4 The ResNet and U-net

The network designed in this thesis contains the main idea of the ResNet and the U-net. The networks and their variants are briefly introduced in this section.

3.4.1 The ResNet

From experience, the depth of the network is critical to the performance of the model. When the number of network layers is increased, the network can extract more complex feature patterns, so theoretically better results can be obtained when the model is deeper. In fact, in addition to the problem of gradient disappearance or explosion, there is also the problem of degradation of deep networks which refers to the phenomenon that deep neural network is sensitive to the small changes and make it very difficult to converge (Duvenaud et al. 2014).

Kaiming He (He et al. 2016) proposed residual learning to solve the degradation problem. For a stacked layer structure (stacked by several layers), when the input is x, its learned features are recorded as $H(x)$. Now we hope that it can learn the residual $F(x) = H(x) - x$. In fact, the original learning characteristics are $F(x) + x$. For example, in the division of 13 by 5 we have $13 = 2 \times 5 + 3$, 3 is the remainder. The 2×5 can be seen as the learned feature, 13 is the input and $2 \times 5 - 13 = -3$ is the residual. However, in the division of 13 by 5 and 14 by 5 gives the same quotient(learned feature), the way that they differ from each other is the different residuals. Residual learning is easier than direct learning of original features. The structure of residual learning is shown in Figure 3.11. This is similar to a "short circuit" in a circuit, so it is called a short-cut connection.

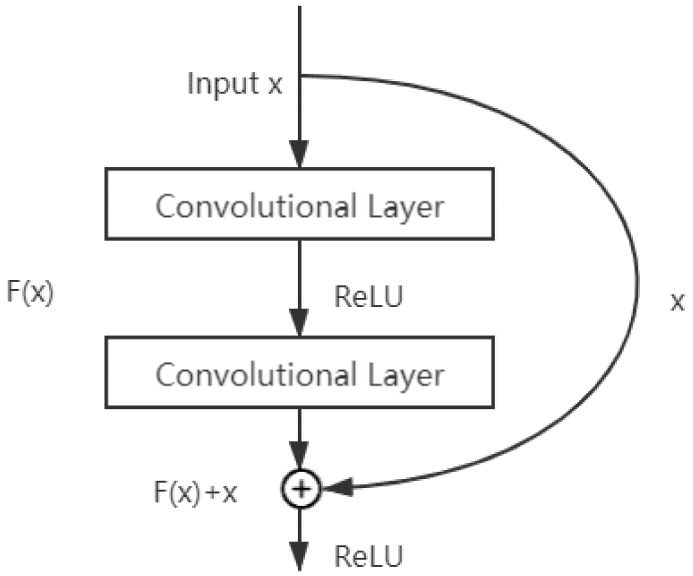

Figure 3.11 *The schematic diagram of a short-cut unit.*

3.4.2 The U-net

U-Net (Ronneberger, Fischer, and Brox 2015) is one of the earliest algorithms for semantic segmentation using fully convolutional networks. The symmetric U-shaped structure containing compression paths and expansion paths was very innovative at the time and affected some of the later designs of the networks for image segmentation. The name of the network is also derived from its U-shape.

U-Net's U-shaped structure is shown in Figure 3.12. The network is a classic fully convolutional network (that is, there is no fully connected operation in the network). The input of the network is an 572×572 input image tile with a mirror operation on the edges. The left side of the network (red line) is a series of downsampling operations consisting of convolution and max-pooling. This part is called contracting path. The compression path is composed of 4 blocks. Each block uses 3 effective convolutions and 1 Max Pooling downsampling. After each downsampling, the number of feature maps is multiplied by 2, so we have the feature map size changed as shown in the figure. The result is a feature map with the size 32×32.

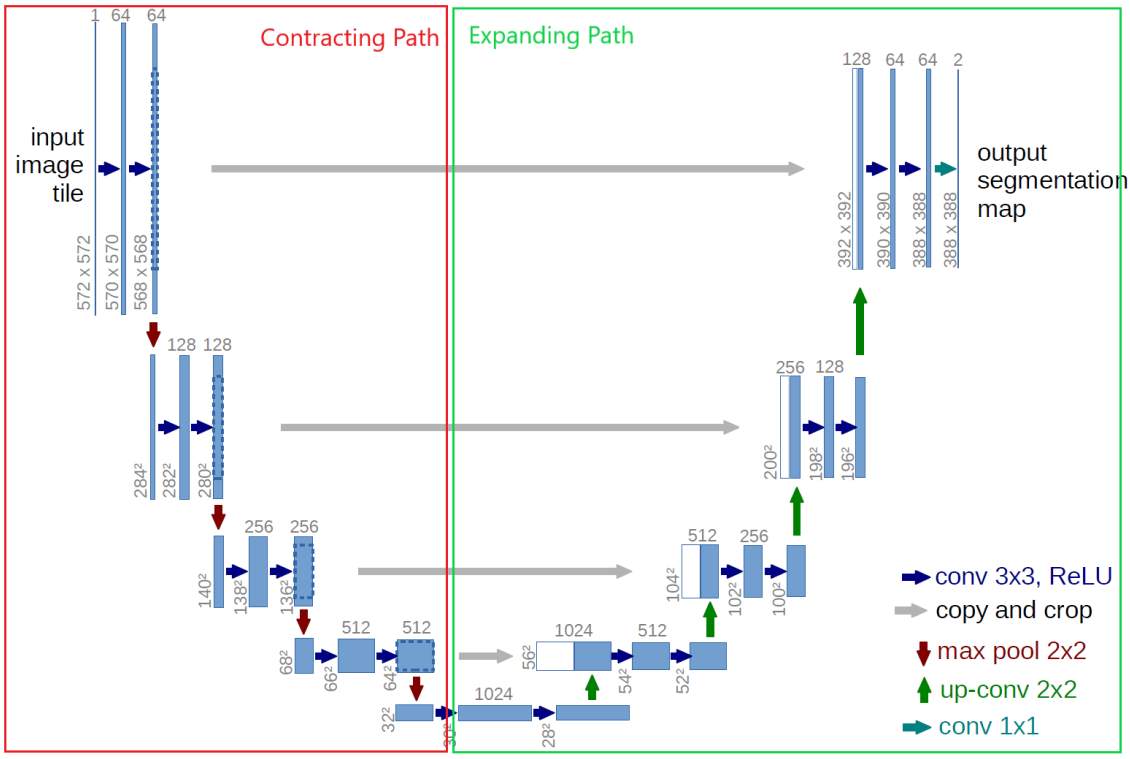

Figure 3.12 *The architecture of the U-net*[1].

The right part of the network (green line) is called the expansion path in the paper. It also consists of 4 blocks. Before the start of each block, the size of the

[1]https://lmb.informatik.uni-freiburg.de/people/ronneber/u-net/

feature map is multiplied by 2 and the number is halved at the same time (the last layer is slightly different). Then the feature map concatenates with the feature map of the symmetrical compression path on the left. Because the size of the feature map on the left compression path and the right expansion path are not the same, U-Net is normalized by cutting the feature map of the compression path to the feature map of the same size as the expansion path. The convolution operation of the extended path still uses the effective convolution operation, and the size of the resulting feature map is 388×388. Since this task is a binary classification task, the network has two output feature maps. Valid padding increases the difficulty and universality of model design, so U-Net uses a loss function with boundary weights. This thesis will not go into details here.

The merge operation in the U-net is to concatenate two matrices in the last dimension. It can be seen as a long skip connection. The merge operation in the ResNet is a simple add operation, it adds the corresponding elements in two matrices. It can be seen as a short skip connection. It is proved that both short and long skip connections (Drozdzal et al. 2016) are important in biomedical image segmentation.

3.4.3 The 3D-U-Net and V-net

3D U-Net (Çiçek et al. 2016) is based on the previous U-Net structure. The difference is that all 2D operations are changed to 3D operations. At the same time, batch normalization is used in order to speed up convergence and avoid training bottlenecks. During training, it is normalized and standardized according to the current batch information. At the same time, compared with U-Net, a weighted softmax loss function is used, and the weight of unlabeled pixels is set to zero, and only the labeled pixels can be learned. The weight in the softmax loss expression of the background is reduced, and the weight of the foreground is increased.

The entire network of V-net (Milletari, Navab, and Ahmadi 2016) is divided into compression paths and uncompression paths, that is, feature maps are reduced and expanded as Figure 3.13. Each stage reduces features by half, and residual learning is added to each stage to accelerate convergence.

The circle and cross in Figure 3.13 represent a convolution with a convolution kernel of $5 \times 5 \times 5$ and a stride of 1. It can be seen that padding $2 \times 2 \times 2$ can keep the feature size unchanged. At the end of each stage, a convolution kernel of $2 \times 2 \times 2$ and a stride of 2 are used. The feature size is reduced by half (the advantage is that there is no need to save pooling switches, so the smaller memory footprint). The entire network uses the PReLU (He et al. 2015) nonlinear unit. A $1 \times 1 \times 1$ convolution is added to the end of the network,the data is processed as the same size as the input and finally a softmax function is applied.

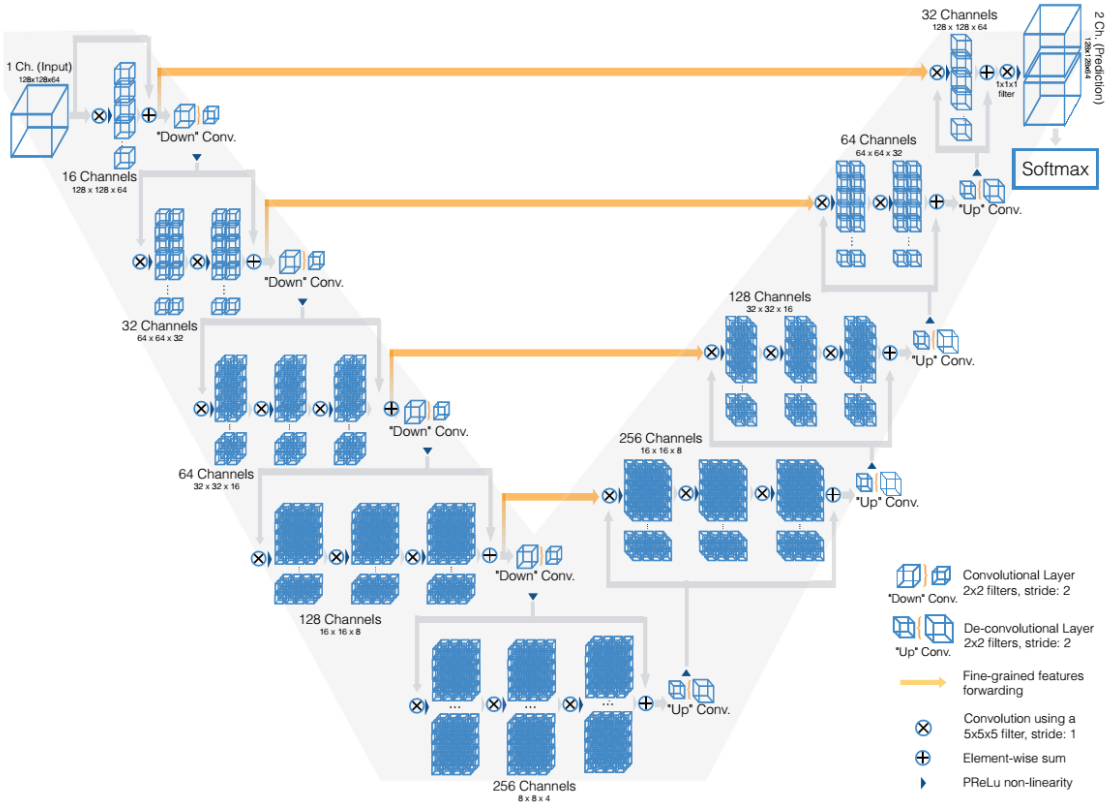

Figure 3.13 *The architecture of the V-net (Milletari, Navab, and Ahmadi 2016).*

The network learns the idea of U-Net, and sends the underlying features of the reduced end to the corresponding positions of the enlarged end to help reconstruct high-quality images and accelerate model convergence. It uses the dice loss instead of the loss used by the U-net. The 3D-U-Net and V-Net shows two different directions of development in 3D image processing. The U-Net kept the original architecture and optimized the distribution in each layer as well as the training method. While the V-Net changed the architecture by adding to new components (residual units).

4 Data

In this chapter, the sources and types of the datasets used in this thesis are introduced. According to the purpose of usage, the datasets can be divided into two parts. A set of images is used for doing binary segmentation and a group of images is used to do multi-class segmentation.

4.1 The binary segmentation

The dataset is a part of the Leukoaraiosis And DISability (LADIS) Study (Waldemar 2002). The study followed patients for three years and took their MRI images (T1-, T2-, proton density-weighted and FLAIR (Fluid-Attenuated Inversion Recovery) pulse sequences) as well as their physical indicators. In this thesis, FLAIR images from 606 patients and the images of manually segmented white matter hyperintensity area are used. Below there are two examples of a slice of the images.

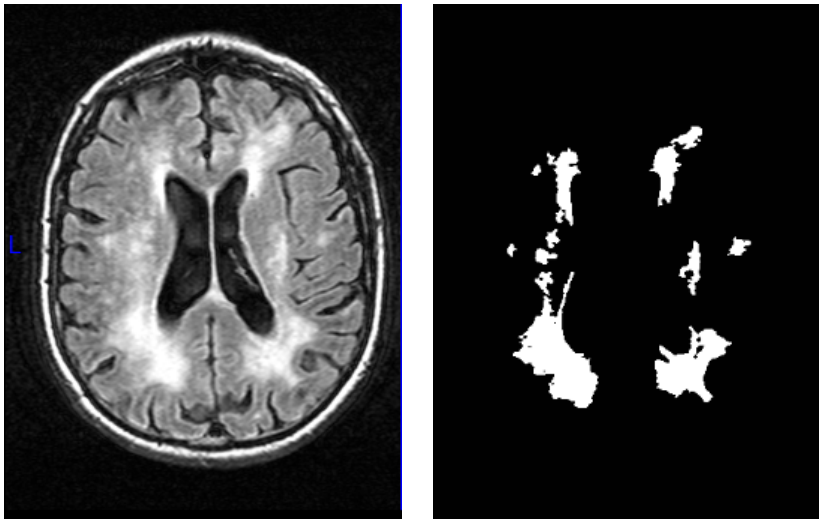

(a) FLAIR image example. (b) White Matter Hyperintensity example.

Figure 4.1 *An example of the FLAIR image and the manual segmentation of white matter hyper-intensities from the corresponding axial slice.*

The Figure 4.1(a) is an axial slice of the FLAIR image. The original FLAIR images contain not only the brain tissues but also the non-brain areas. The non-brain areas do not contribute to the brain segmentation. They are irrelevant features or noise features, Especially in T1 images, the intensity of eyes is similar to some brain tissues. The non-brain areas will extend the total training time, decrease the model accuracy and increase the risk of overfit. A brain mask (Lötjönen, Robin

Wolz, Koikkalainen, Julkunen, et al. 2011) can be generated by atlas-based method from T1 images. It is a 3D image with values 0 and 1 only. Value 0 stands for non-brain area and value 1 stands for brain area. Use the brain mask on all the FLAIR images and T1 images, this process is called skull-stripping. Originally, the thickness of one FLAIR slice is about 6mm. Processed so that all the images are spatial normalization to same space with 1 mm isotropic space with size of $180 \times 256 \times 256$ and values are z-score normalized with zero mean and standard deviation equals to 1. The manually labeled images have the same size as the FLAIR images. In the manually segmented images, all the WMH areas are labeled as 1 and the background is labeled as 0. Table 4.1 compared the two images after pre-processing.

Table 4.1 *Binary segmentation training data and testing data.*

	FLAIR images	**label images**
quantity	606	606
size	180*256*256*1	180*256*256*1
value range	mean=0, std=1	{0,1}
type	gray-scale	gray-scale
use	training data	ground truth
feature	WMH is brighter than normal white matter	label 0 is the background label 1 is the WMH

4.2 The multi-region segmentation

It is extremely time consuming to generate large number of training samples with different brain regions segmented manually. Consequently, an alternative approach was selected in this thesis. A dataset of 1151 MRI images is generated by utilized an atlas-based segmentation method (Lötjönen, Robin Wolz, Koikkalainen, Thurfjell, et al. 2010). This method segments automatically the T1 images into 139 brain regions. The T1-weighted images were used as training set and the automatic segmentations as the ground truth. Figure 4.2 shows a T1 image from a patient and its segmentation. Different colors in Figure 4.2(b) stand for different brain regions.

The automatically generated dataset contains segmentation errors. In order to test the performance of the network on manually segmented data, we prepared 80 T1-weighted images and the manually labeled results made by medical experts.

In addition to producing accurate segmentation, it is important that the automatically generated segmentations are consistent. Therefore, a dataset from 20 patients that had two T1 images acquired during the same time was used. Also, the manual segmentations were available for both images. The difference between the results from one person shows the consistency of the model. The two sets of slices in Figure 4.3 are nearly the same except some system errors and random errors.

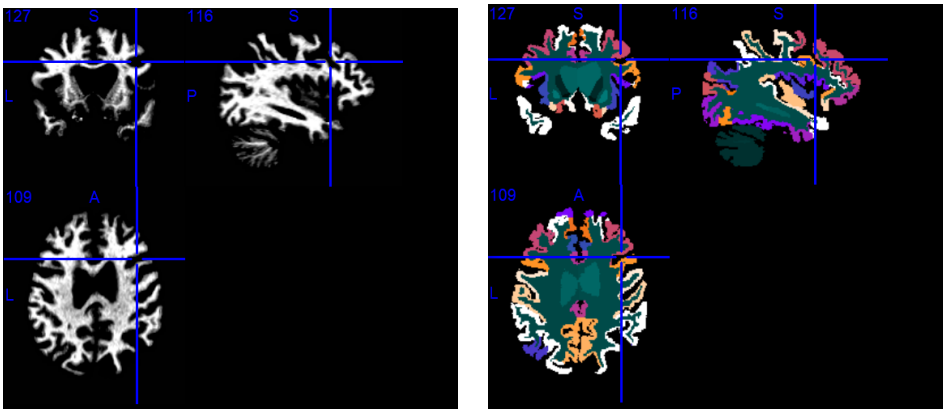

(a) T1 image example.

(b) Segmentation from atlas-based segmentation.

Figure 4.2 *An example of T1 image and its atlas-based segmentation result.*

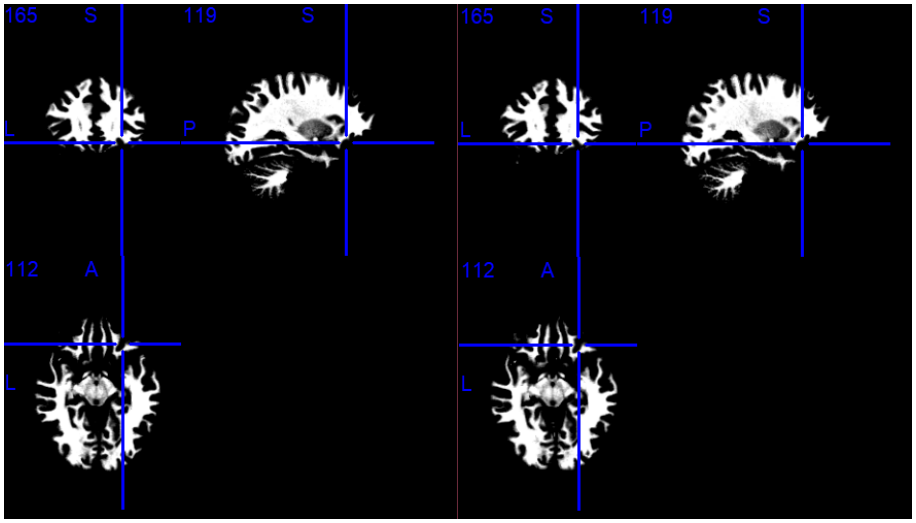

Figure 4.3 *The two T1 images from one patient from the consistency dataset.*

A brief summary of the data used in the multi-region segmentation is listed in the Table 4.2.

In the ground truth from both manual data (data segmented by expert) and automatic data (data segmented by atlas-based method) the value range is a set of 140 values from 0 to 139. Index 0 stands for the background and all the rest 139 numbers are the indexes of brain regions. Most brain regions appear both in the left brain and the right brain, so the area on the left and right is marked with two indexes separately. Some regions like cerebellum are located in the middle of the brain, so only one index is given to the region like this. The Table 4.3 shows the position and index of each region.

Table 4.2 *The summary of the three datasets.*

	Atlas-based segmentation dataset	**Manual segmentation dataset**	**Consistency dataset**
quantity (T1, GT)	1151 ,1151	80, 80	40, 40
size	180*256*256*1	180*256*256*1	180*256*256*1
value range (T1, GT)	[0,1], {0,1...139}	[0,1], {0,1...139}	[0,1], {0,1...139}
type	gray-scale	gray-scale	gray-scale
use	training and validating	training and validating	consistency testing
source	the GT is generated by atlas-based method	the ground truth is manually labeled	
feature	In the ground truth, the area with label 0 is the background and label 1-139 are different brain regions.		the two images from one patient should have the same result

Table 4.3 *The indexes, positions, and names of the 139 brain regions.*

position	**name**	**left**	**right**
Ventricles	3rd ventricle	1	
	4th ventricle	2	
	5th ventricle	3	
	Inferior lateral ventricle	23	22
	Lateral ventricle	25	24
Deep gray matter	Accumbens area	5	4
	Caudate	10	9
	Pallidum	27	26
	Putamen	29	28
	Thalamus proper	31	30
Temporal Lobe	Amygdala	7	6
	Hippocampus	21	20
	Entorhinal area	57	56
	Fusiform gyrus	63	62
	Inferior temporal gyrus	69	68
	Middle temporal gyrus	91	90
	Parahippocampal gyrus	105	104
	Planum polare	115	114
	Planum temporale	119	118
	Superior temporal gyrus	133	132
	Temporal pole	135	134
	Transverse temporal gyrus	139	138

Miscellaneous	Brain stem	8	
	Cerebral exterior	16	15
	Cerebral white matter	18	17
	CSFnm	19	
	Ventral diencephalon	33	32
	Vessel	35	34
	Optic chiasm	36	
Occipital Lobe	Calcarine cortex	51	50
	Cuneus	55	54
	Inferior occipital gyrus	67	66
	Lingual gyrus	71	70
	Middle occipital gyrus	81	80
	Occipital pole	93	92
	Occipital fusiform gyrus	95	94
	Superior occipital gyrus	129	128
Cerebellum	Cerebellum exterior	12	11
	Cerebellum white matter	14	13
	Cerebellar vermal lobules I-V	37	
	Cerebellar vermal lobules VI-VII	38	
	Cerebellar vermal lobules VIII-X	39	
Frontal Lobe	Basal forebrain	41	40
	Anterior cingulate gyrus	43	42
	Anterior insula	45	44
	Anterior orbital gyrus	47	46
	Central operculum	53	52
	Frontal operculum	59	58
	Frontal pole	61	60
	Gyrus rectus	65	64
	Lateral orbital gyrus	73	72
	Middle cingulate gyrus	75	74
	Medial frontal cortex	77	76
	Middle frontal gyrus	79	78
	Medial orbital gyrus	83	82
	Precentral gyrus medial segment	87	86
	Superior frontal gyrus medial segment	89	88
	Opercular part of the inferior frontal gyrus	97	96
	Orbital part of the inferior frontal gyrus	99	98
	Posterior orbital gyrus	113	112

	Precentral gyrus	117	116
	Subcallosal area	121	120
	Superior frontal gyrus	123	122
	Supplementary motor cortex	125	124
	Triangular part of the inferior frontal gyrus	137	136
Parietal Lobe	Angular gyrus	49	48
	Postcentral gyrus medial segment	85	84
	Posterior cingulate gyrus	101	100
	Precuneus	103	102
	Posterior insula	107	106
	Parietal operculum	109	108
	Postcentral gyrus	111	110
	Supramarginal gyrus	127	126
	Superior parietal Lobule	131	130

5 Method

The work flows for both binary segmentation and multi-region segmentation are roughly the same. In general, it contains three parts: image pre-processing, model training and result post-processing. In this chapter, the methods of performing segmentation on different types of datasets are proposed.

5.1 Preprocessing

The preprocessing procedures for FLAIR images and T1 images are slightly different. The work flows are listed in the Figure 5.1 below.

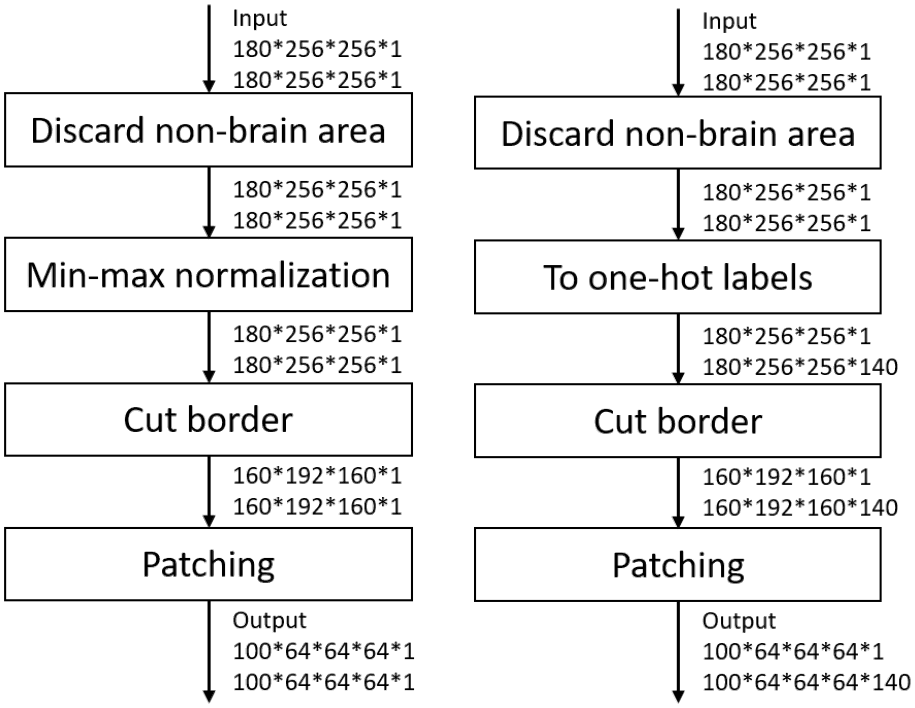

(a) Preprocessing of FLAIR. (b) Preprocessing of T1.

Figure 5.1 *Preprocessing work flows.*

Factors such as the patient location in the scanner, the scanner itself, and many unknown issues can cause differences in brightness on the MR image. In other words, the intensity value (from black to white) can vary within the same tissue. This is called a bias field. Bias fields cause non-uniformities in the magnetic field of the MRI machine. If the offset field is not corrected, all imaging processing algorithms will output incorrect results. Before segmentation or classification, a pre-processing

step is required to correct the effect of the bias field. An N4 bias field correction tool(Avants, Tustison, and Song 2009) is applied to all the images.

The min-max normalization method (Equation 3.11) is applied to the FLAIR images. Hence, all the values in images are in interval [0,1]. No need to normalize the values in T1 images because they falls in the $[0, 1]$ interval naturally. For the label images of T1 images, The label is changed to one-hot vectors, so the dimension is changed from $180 \times 256 \times 256 \times 1$ to $180 \times 256 \times 256 \times 140$. The last dimension of the ground truth images indicates the class that a voxel belongs to. In the matrix, only voxels that belong to class i are labeled as 1 and 0 otherwise. Class 0 is the background and classes 1, 2, ... 139 are different brain regions shown in Table 4.3.

Class imbalance of data is often encountered in machine learning, also known as class skew. It also happened in the images used in this thesis. For instance, in binary segmentation, the number of voxels of WMH is 20000 in average. The total number of voxels in a FLAIR images is over 10^7. If the system predicts all the voxels as background, that is it wrong predicts all the true cases, the accuracy is still over 99%. Therefore, it is meaningless to measure a model with its accuracy. The most straightforward method to solve the imbalance problem is to make the data balanced. The border containing background only is discarded. Then the size of the image shrinks to $160 \times 192 \times 160$. The data is more balanced than before but it is still far from half to half.

During the CNN learning and training process, instead of processing an entire image at a time, the image is first divided into multiple small blocks. The kernel (or filter or feature detector) only views one block of the image at a time. The small block is called a patch, and the filter is moved to another patch of the image, and so on. The CNN kernel(filter) processes only one patch at a time, not the entire image. This is because we want the filter to process small patches of the image in order to detect features (edges, etc.) within the GPU memory limitation. This also has a good regularization property, because the number of parameters we estimate is small, and these parameters must be ”good” in many areas of each image (Z. Yan et al. 2017).

For a simple CNN, the size of the patch that minimizes information loss is the size of the receptive field. The receptive field (Dumoulin and Visin 2016) can be briefly defined as the region in the input space that a particular CNN's feature is looking at. For a 2D convolutional layer with a 3×3 filter, each pixel in the output corresponds to a 3×3 area in the input. Thus, the receptive field is 3×3. In spite of this fact, as the size of the receptive field increases with the number of neural network layers, the size of the receptive field is close to the size of the whole image. Under these circumstances, the size of a patch has to be smaller than the receptive field with some information loss.

The methods(Figure 5.2) used in both binary segmentation and multi-region segmentation to generate training patches are the same. In three directions x, y and z, a $64 \times 64 \times 64$ patch for every 32 voxels was generated. That is, when the MRI image is a $160 \times 192 \times 160$ sized big cube, there is a small window the size of which is $64 \times 64 \times 64$. The window can slide freely inside the big cube from a corner of the cube. Every time the window can only slide in one direction. Every time the window slides a length of 32 units, it generates a smaller cube that has the same size as the window.

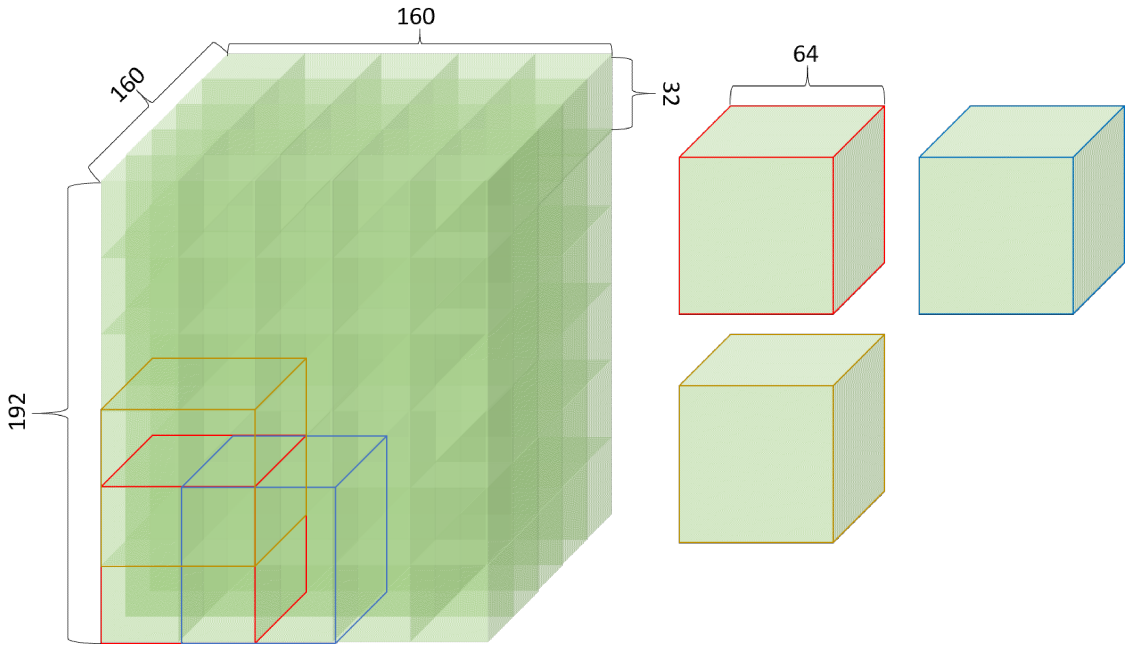

Figure 5.2 *The MRI image with three patches generated.*

It is easy to count that from each $160 \times 192 \times 160$ sized image, a number of $4 \times 5 \times 4 = 80$ patches can be produced. Over-sampling can help to make the data more balanced. There are other 20 patches randomly generated from the inner area of the image which is labeled red in Figure 5.3. The size of the inner area is $96 \times 128 \times 96$. The WMH is more likely to appear in this area, so the proportion of true cases is higher than in the whole image.

5.2 Model selection and training

5.2.1 The binary segmentation

A 3D image can be seen either as a simple 3D image or as a set of 2D images. For instance, a 3D image with the size of $160 \times 192 \times 160$ can be seen as 160 192×160 2D images, each 2D image is a slice on the z axis. Figure 5.4 explains the process.

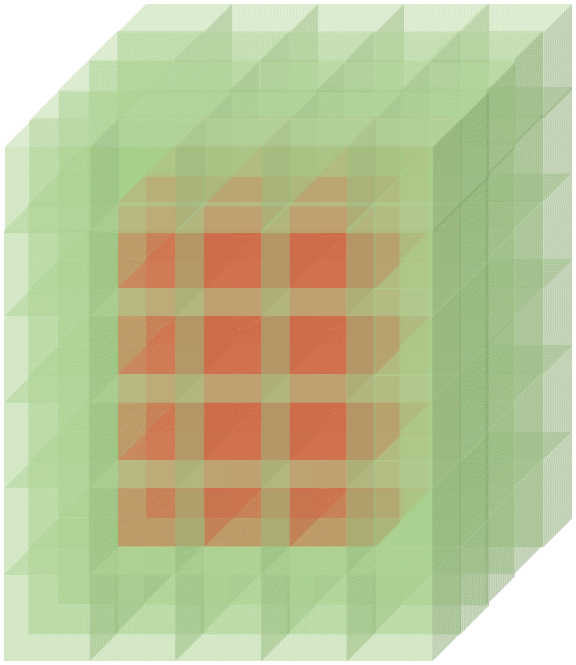

Figure 5.3 *The red area shows the region from where the random patched are generated.*

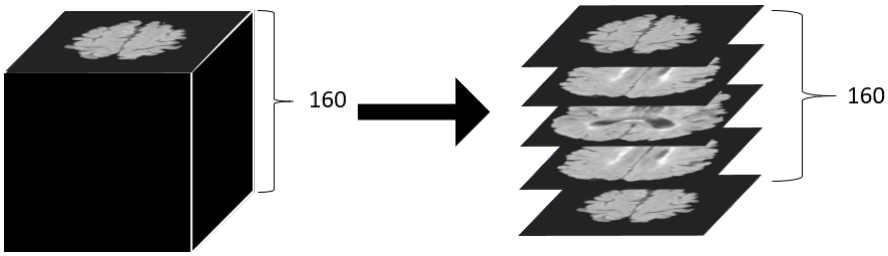

Figure 5.4 *The 3D to 2D process.*

As the inputs are 2D images rather than 3D images, the network contains 2D convolution layers and 2D deconvolution layers only. It saves training time, simplifies the computation and reduces the memory usage. To compare the performance of 2D inputs and 3D inputs, a simple encoder and decoder network without patching is built.

Note that when the 3D image is transformed to a group of 2D images, the 2D images in a group are ordered. So as to let the network learn about the sequential information, the images in the group should not be shuffled and the size of the batch should be set as the quantity of the images from one 3D image. This sacrifices some generalization performance of the model, but learns more information from each group of images.

The model as simple as the one in Figure 5.5 is not sufficient to learn all the features, but a deeper network is needed. With the inspire of the U-net, a 3D U-

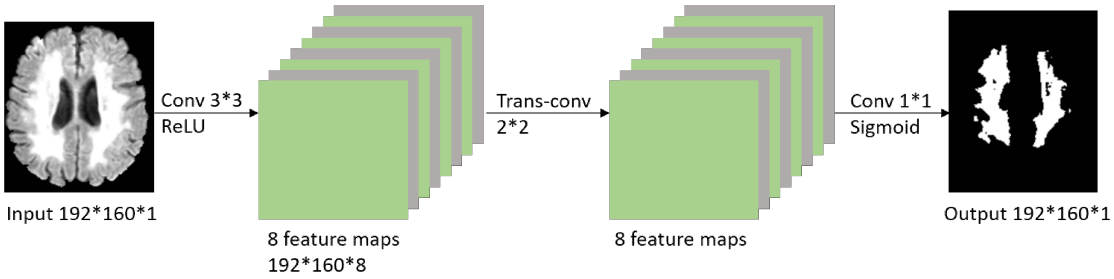

(a) One-layer network with 2D input.

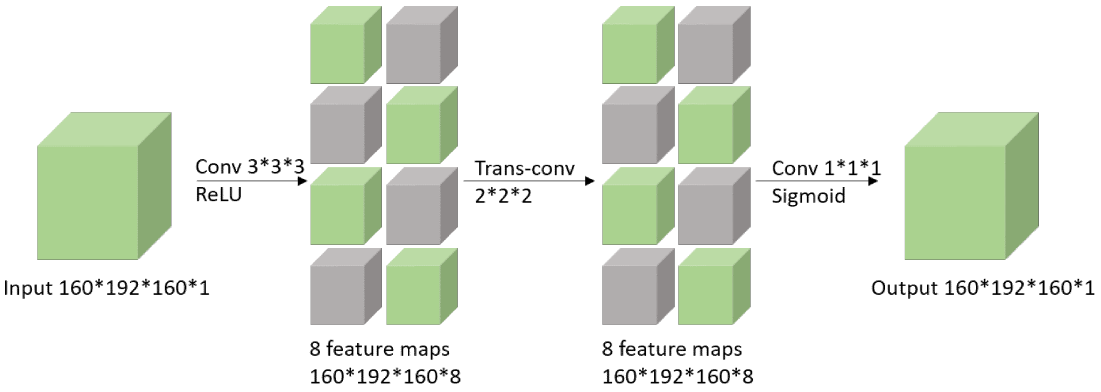

(b) One-layer network with 3D input.

Figure 5.5 *The one-layer models.*

net with long connection only and batch normalization but still without patching is created (Figure 5.6).

The network in Figure 5.6 has four compressing layers and four decompressing layers. In each compressing layer, the convolution is done twice with batch normalization and activation. Two compressing layers are connected with a max-pooling operation. After the max-pooling, the length, width and depth in each feature map are halved. In each decompressing layer, a transposed convolutional layer doubles the length, width and depth in each feature map but halves the quantity of feature maps. Then the feature maps are concatenated to the feature maps with the same dimensions that were generated from the compressing layers. Afterwards, the above steps (two convolutional layers) in the compressing layers are repeated in decompressing layers. Finally, Sigmoid activation method is used to give the output.

Instead of using long skip connection only, merging the network in Figure 5.6 with the short cut in Figure 3.11 will give a different network shown in Figure 5.7(a) and Figure 5.7(b). Giving different inputs (use patching or not) the necessary of patching can be tested.

In the networks shown in Figure 5.7(a) and Figure 5.7(b), the only difference is the size of each feature map. They contain four compressing layers and four

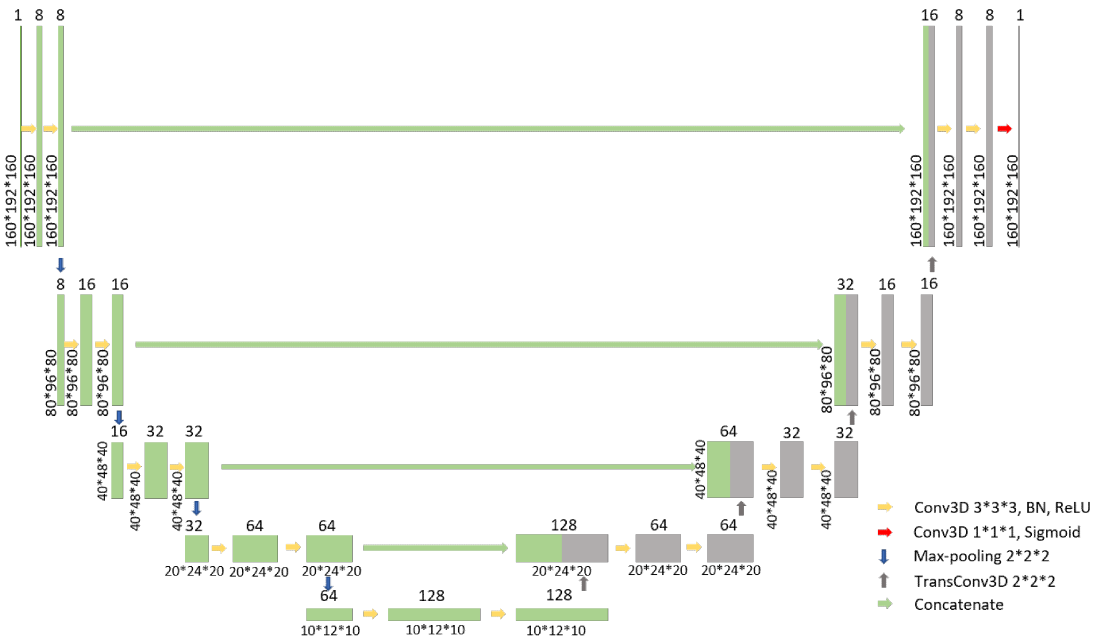

Figure 5.6 *The basic 3D U-net with no patching.*

decompressing layers as well but the operations in each layers are different from the layers in Figure 5.6. In the first three compressing layers, there are two convolutional layers with kernels size of 3×3 and 1×1 that are used to extract the features from the image. Then we normalize both results and sum the two results together. The result from 3×3 kernel is the learned feature and the result from 1×1 kernel can be seen as the residual. The sum of two results is activated by ReLU and passed to the next layer. In the last compressing layer and the first three decompressing layers, after the two results from kernels size of 3×3 and 1×1 are added together and activated. Finally a dropout layer with the dropping rate of 0.5 is added at the end. While in the last decompressing layer there is no dropout layer, the operation is the same as the first four compressing layers, except the 1×1 convolutional layer with a Sigmoid activation layer to get the output.

5.2.2 The multi-region segmentation

There are only two classes in the binary segmentation and the two classes are labeled as categorical (0 and 1) by default. Conversely, the labels are numerical in the multi-region segmentation. After changing the labels to one-hot labels, the dimension of the ground truth is changed from $160 \times 192 \times 160 \times 1$ to $160 \times 192 \times 160 \times 140$. Such a big matrix is not suitable to be passed to the network entirely due to the limitation of GPU memory and computation ability. There is no choice but to do patching. The main structure should be very similar to the network in Figure 5.7(b). In order

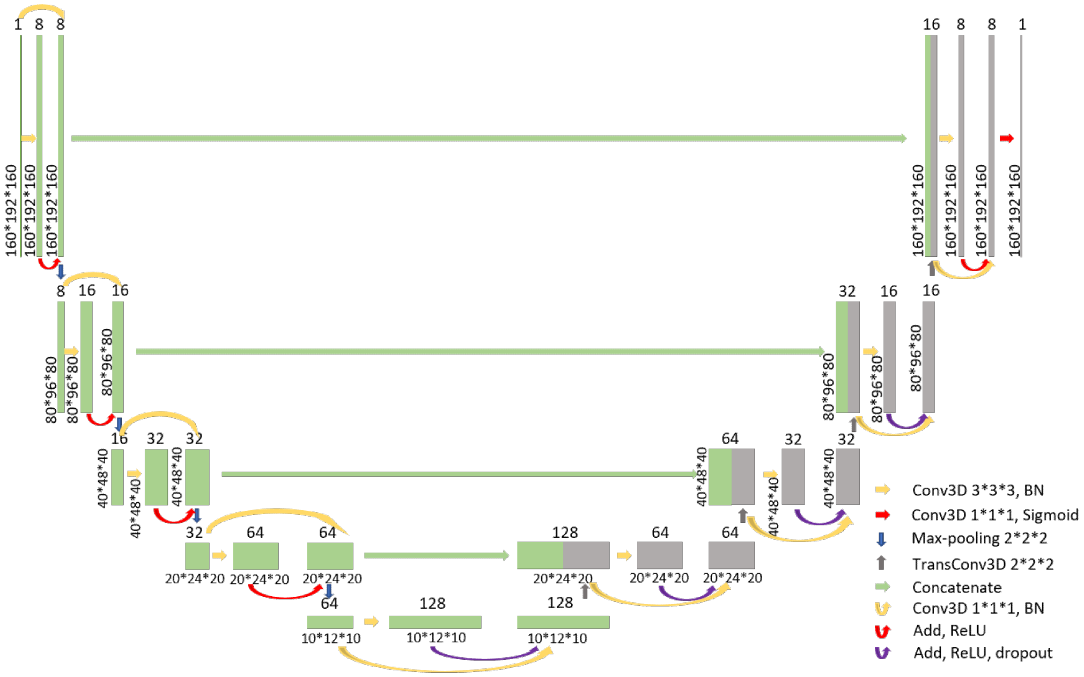

(a) The 3D U-net with no patching but with short cut.

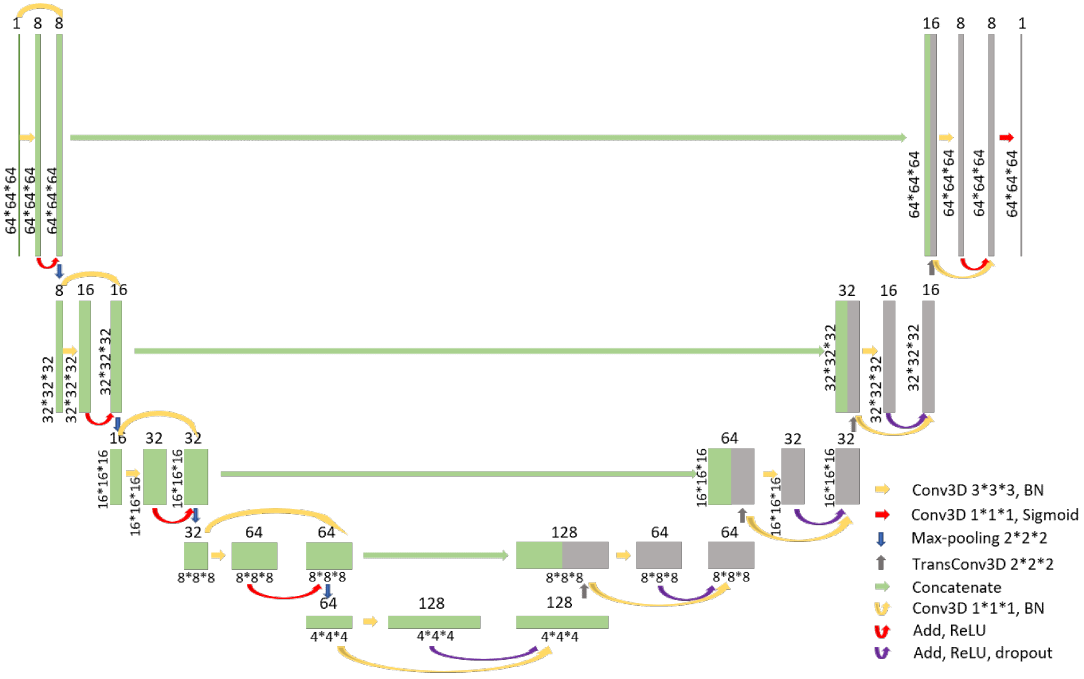

(b) The 3D U-net with both patching and short cut.

Figure 5.7 *The models with both long and short skip connections.*

to make the output contains 140 dimensions, the final layer should be with 140 feature maps instead of one and the activation function should be Softmax instead of Sigmoid.

In the paper of Inception V3 (Szegedy et al. 2016), the authors introduced four general design principles in network designing. The second one says that the number of feature maps should increase gently. The increment of feature maps from 8 to 140 is so sharp that may cause information loss. In this thesis, a test of setting the initial number of filters as 8, 16 and 32 is designed. Figure 5.8 is the schematic diagram of the multi-region segmentation network with 32 filters initially.

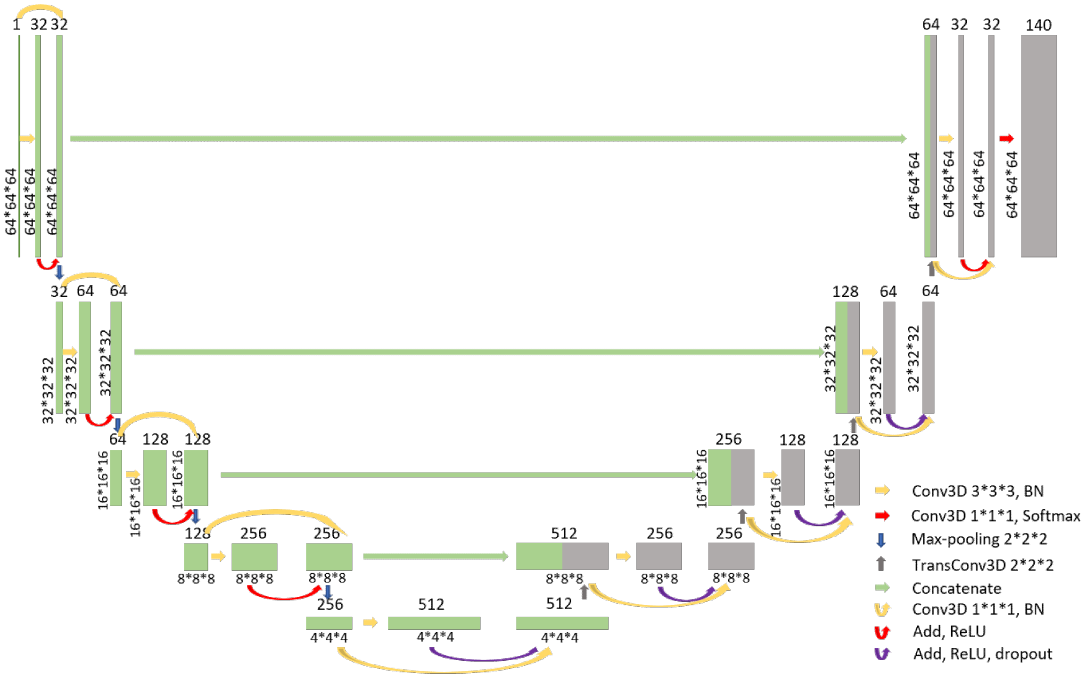

Figure 5.8 *The 3D U-net for the multi-region segmentation.*

5.3 Post-processing

For the networks with whole images as input, there is no further post-processing procedure needed. However, for the networks with patches as input, the patches should be merged into a whole image. In order to save time, the testing images are split into non-overlapping patches.

The image on the left side in Figure 5.9 has a size of 160×192 and it can be changed to nine 64×64 patches. The side with length of 192 can be divided by 64 easily but the other side can be divided to 2.5 patches only. The network only accepts full sized patches. To solve this problem, the image will be divided into 9 patches (6 red ones and 3 green ones), the red ones can be merged together while for the green ones, only the right half of each patch participates the merging process.

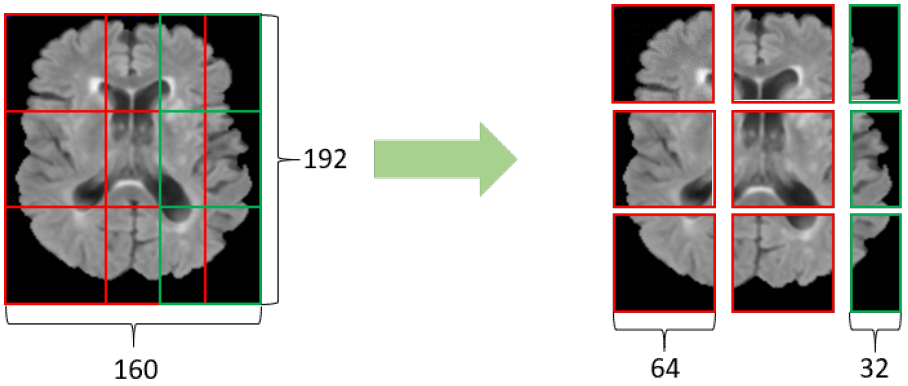

Figure 5.9 *The non-overlapping patching method.*

An $160 \times 192 \times 160$ sized image can be changed to 27 $64 \times 64 \times 64$ patches with the same mechanism. This method can be used in the binary segmentation but not in the multi-region segmentation.

The mechanism above assumed that the location of a voxel in a patch does not influence the predicting accuracy, that is, a voxel can be included in several different patches and the prediction result for this voxel in all the patches should be the same. This is a wrong assumption. Due to the zero-padding applied to the convolutional layers and transformed convolutional layers, the probability of a prediction is the maximum value in the softmax result. The probability can be seen as a 3-variate normal distribution in a 3D patch. Anyway the probability is not a uniform distribution.

Class name	1	2	3	4	5	6	…
probability	0.07	0.12	0.05	0.7(max)	0.01	0.03	…

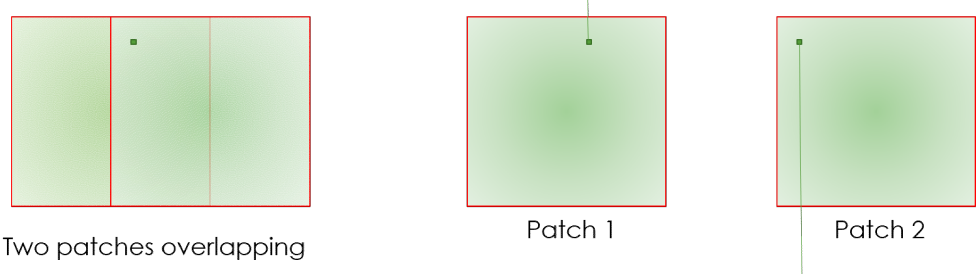

Class name	1	2	3	4	5	6	…
probability	0.01	0.3(max)	0.05	0.1	0.01	0.01	…

Figure 5.10 *A non-quantitative overlapping patching example.*

Figure 5.10 shows two overlapping patches, the probability for the selected pixel in patch 1 is 0.7 and the certainty in patch 2 is 0.3. The probabilities for pixels are

not the same in a patch. Here it is assumed that the patch is more certain about the darker area and less certain about the lighter area. For the selected pixel in the overlapping area, it is contained by both patches. The table above is the softmax result from patch 1 and the table below is the softmax result from patch 2. The result from patch 1 shows that this pixel has the probability of 0.07 to be classified as class 1, 0.12 as class 2 and so on. The highest probability is 0.7 for class 4 ,so the patch will predict the pixel as class 4. In patch 2, the highest probability is 0.3 for class 2 so the pixel will be predicted as class 2. There is no doubt that $0.7 > 0.3$ which means patch 1 is more sure about the result. Therefore, the pixel will be predicted as class 4. If this idea is used in model choosing, it is so called soft voting in ensemble learning (H. Wang et al. 2013). Another possibility is to compute the mean of the probabilities. However, it increases the computation especially for the cases with more than two patches overlapping. According to the experiment, no significant difference is shown by taking the maximum or mean.

Under 2D condition, with the patches size of 64×64 pixels, there can be at most four patches overlapping and the overlapping area is 32×32 pixels. Under 3D condition (see Figure 5.11) each $32 \times 32 \times 32$ sub-patch (the red cube) can be surrounded by 8 $64 \times 64 \times 64$ patches at most. Those sub-patches located in the border or the corner can only be surrounded by 1,2 or 4 patches.

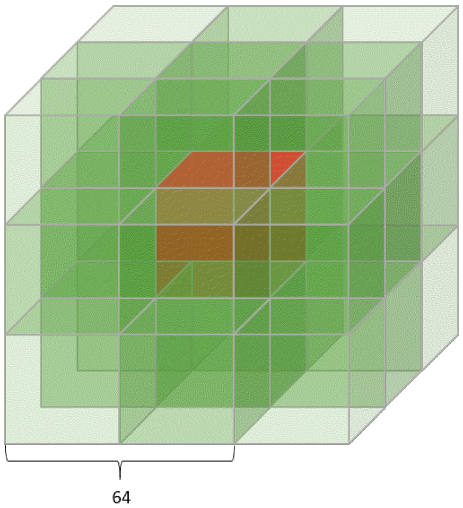

Figure 5.11 *A 3D overlapping patching example. Eight 3D patches overlap and the red area is contained by all the 8 patches. For other areas, the more patches overlap, the darker the color is.*

An $160 \times 192 \times 160$ sized image contains $4 \times 5 \times 4 = 80$ patches size of $64 \times 64 \times 64$. The 80 patches as segmented as the same way as in Figure 5.2. Each voxel is voted by the patches containing it. After then, the shape of the output is back to $160 \times 192 \times 160 \times 1$ and can be compared with the ground truth.

6 Results

Tests are done separately for the binary segmentation and the multi-region segmentation.

The tools and platforms used in the experiments are shown in the Table 6.1.

Table 6.1 *The environment of the experiment.*

name	**version**
system	Windows 10 pro 1909
CPU	Intel Core i7 6700HQ
RAM	16GB
GPU	NVIDIA GTX 1070
Python	3.7.4
tensorflow	1.15.0
Keras	2.3.1
numpy	1.18.1
IDE	Spyder 4.0.1

6.1 The binary segmentation

First, 90% of the FLAIR images and corresponding ground truth images are used as training data, 5% are testing data and the rest 5% are the validating data. The data is chosen randomly.

The one-layer model (see Figure 5.5) is trained in order to compare the performance of 2D inputs and 3D inputs. After 50 epochs with dice loss, the dice score of 2D model converges on 0.34 and the dice score of 3D model converges on 0.60. Such a big difference means that there is no necessary to build a 2D network for WMH segmentation. The Figure 6.1 below is an example of the 3D model with one layer only.

By comparing the Figure 6.1(b) and the Figure 6.1(c), we can find that with one layer only, the result is already very similar to the ground truth. However, due to the lack of network layers, features can not be learnt completely. Therefore the deeper network shown in Figure 5.6 is trained. After 50 epochs with dice loss, the accuracy reaches 99.9% on the training data and 99.7% on the validation data, the dice score reaches 0.79 on the training data and 0.71 on the validation data. The accuracy here indicates the proportion of voxels whose predicted result (0 or 1) is the same as the ground truth value (0 or 1) to the total number of voxels in the ground truth image. However, the performance of this network when doing 10-fold cross validation is not as good as expected. That is, divide all data sets into ten

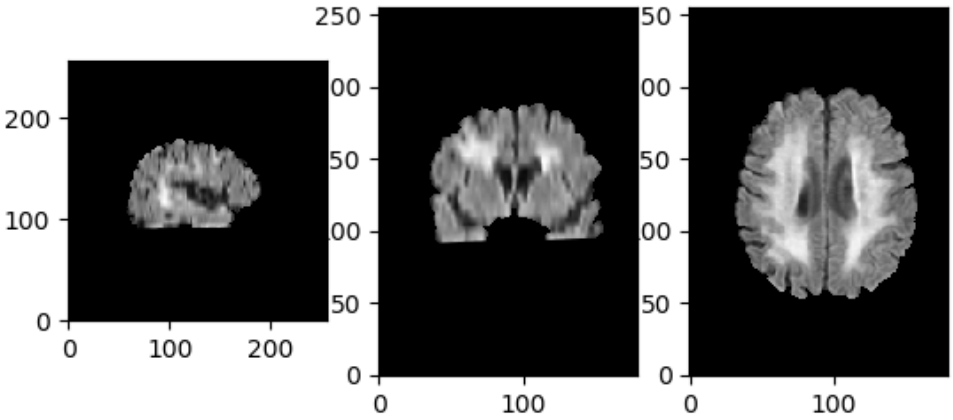

(a) The FLAIR image slices.

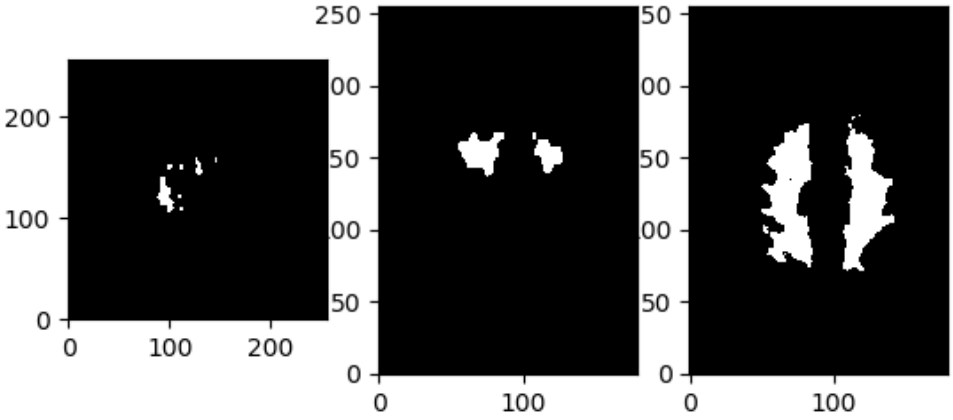

(b) The ground truth image slices.

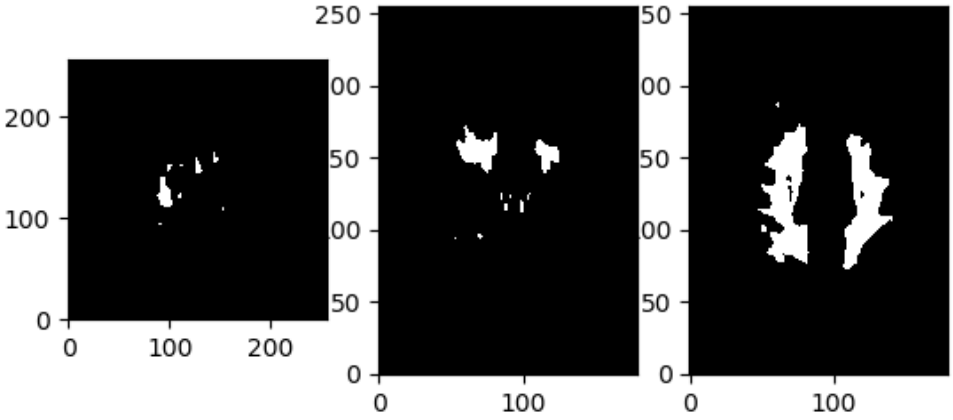

(c) The predict result image slices.

Figure 6.1 *The result of the 3D one-layer model.*

parts, take one of them as the test set, and use the other nine parts as the training set to train the model, and then calculate the model's dice score and accuracy on the test set. This is repeated for ten times. The overall dice score is 0.67 which is less than the result from training which means that the data used in training period might be biased. Table 6.2 summarizes these results.

Table 6.2 *Results from simple models*

	3D deep model				**one-layer 2D model**			**one-layer 3D model**		
	train	**val**	**test**	**10f CV**	**train**	**val**	**test**	**train**	**val**	**test**
acc	0.999	0.997	0.997	0.995	0.998	0.995	0.993	0.998	0.996	0.995
dice	0.804	0.697	0.690	0.674	0.545	0.443	0.411	0.707	0.642	0.622

In the Table 6.2, val stands for validation, acc stands for accuracy and 10f CV is the 10-fold cross validation. In a similar way, a test to show the importance of patching method is achieved by comparing the performances of the networks in Figure 5.7(a) and Figure 5.7(b). By choosing different loss functions the results are shown in the Figure 6.2.

In each of the four subplots, the yellow line is the network in Figure 5.7(b) using the binary cross entropy (BCE) loss function. The blue line is same as the yellow line but using dice loss. The red line and the green line are the network in Figure 5.7(a), the red one uses dice loss while the green one uses binary cross entropy. The main evaluation criteria should be the dice loss rather than the accuracy in the field of medical image segmentation especially in the case that the data is so imbalanced. From the first two subplots, it is shown that the results from patches are better than the results from whole images. The horizontal lines are the mean values of the lines with corresponding colors. The yellow and blue horizontal lines are always above the red and green ones. Therefore, the binary cross entropy works better with patching and the dice loss works better together with whole images. Actually some other loss functions are tested as well, for example the focal loss (T.-Y. Lin et al. 2017) and the weighted cross entropy loss, but the results were unsatisfactory. In the lower two subplots, the two results from non-patching networks are stable on training data but fluctuate a lot on testing data. In other words, the generalization ability of the non-patching model is not good.

To avoid some potential bias associated with head size and brain size, the WMH volumes are converted to ICV% in Figure 6.3 and Table 6.3. The ICV is the total intracranial volume. The ICV% is computed by dividing the volume of the region by the ICV of the patient. Thereafter a comparison can be done with the results from other papers. In the first two linear regression results, the patching method is not used and the loss function is the dice loss. The predicted WMH volume is from 10-fold cross validation and the true WMH volume is from the ground truth

(a) The dice score of training data.

(b) The dice score of testing data.

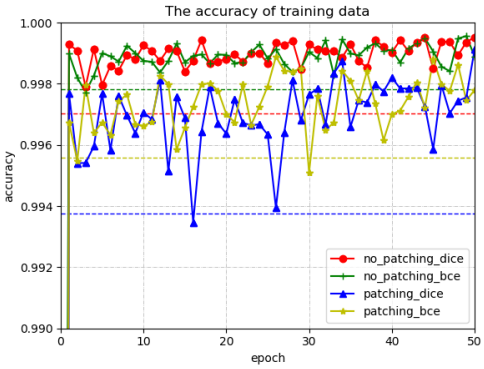

(c) The accuracy of training data.

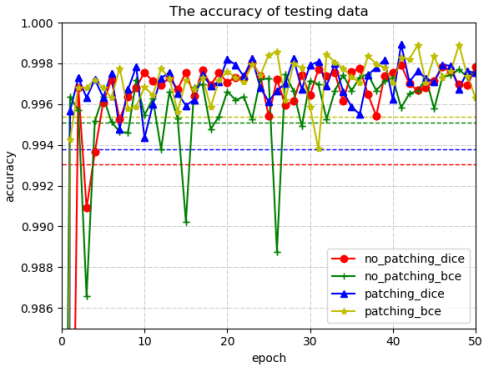

(d) The accuracy of testing data.

Figure 6.2 *The results of the 3D long and short connection models with different loss functions and patching or not.*

labeled by medical experts. The dots in the upper two subplots are more sparse and the lower two are more concentrated to the ideal trend. Each point is the result from a FLAIR image, the abscissa is the real WMH ICV% and the ordinate is the predicted result. From the lower two scatter plots, we can find that binary cross entropy works better than dice loss with patching. There are unavoidable outliers in every results, which might come from manual mistakes when experts were doing segmentation or the system defect.

The rightmost four columns in the Table 6.3 are from the paper (Guerrero et al. 2018). The source of the dataset in that paper is the same LADIS dataset as this thesis, but the author probably chose a different subset from this thesis. The uResNet is a network proposed in that paper. Guerreroet al. compared their uResNet with some automatic segmentation tools (i.e. DeepMedic (Kamnitsas, Ledig, et al. 2017), LPA (Schmidt 2017), LGA (Schmidt et al. 2012)) from several aspects, including the mean and the standard deviation of the dice score, the coefficient of determination(i.e. R^2, see Equation 6.1) and the linear regression of the predicted

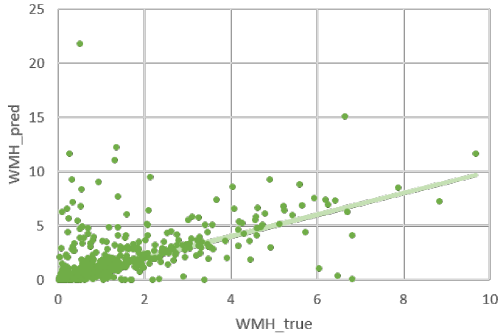

(a) The non-patching long connection only result.

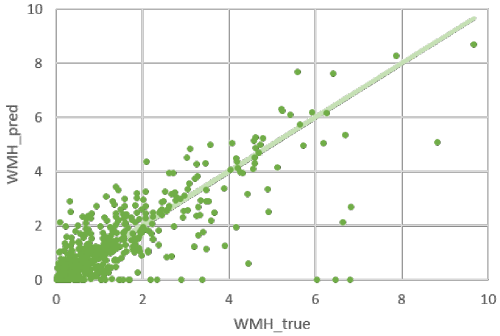

(b) The non-patching long and short connection result.

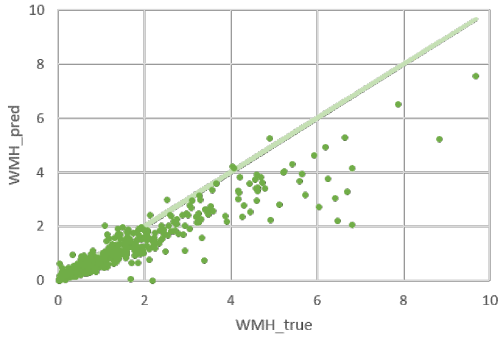

(c) The patching result with dice loss.

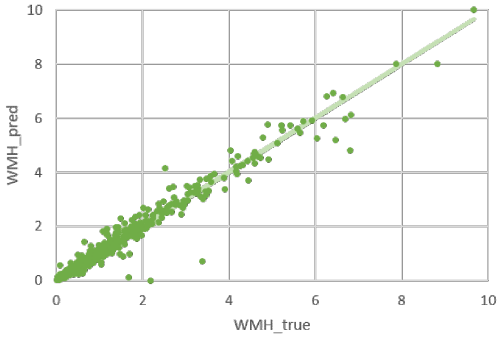

(d) The patching result with bce loss.

Figure 6.3 *The linear regression results. Horizontal and vertical coordinates are in units of ICV%. The green line indicates the ideal trend* $f(x) = 1.0x + 0.0$.

Table 6.3 *Mean Dice scores of WMH (standard deviation in parenthesis) and correlation analysis between expert and automatic volumes (R^2 and trend).*

	no-patching dice loss	**patching dice loss**	**patching bce loss**	**uResNet bce loss**	**Deep Medic**	**LPA**	**LGA**
Dice	0.630	0.710	**0.783**	0.695	0.666	0.647	0.410
(std)	(0.243)	(0.119)	**(0.118)**	(0.161)	(0.167)	(0.190)	(0.229)
R^2	0.352	0.886	**0.964**	0.951	0.943	0.855	0.687
Trend	0.93x	0.68x	**0.98x**	0.89x	0.91x	0.83x	0.51x
	+0.07	+0.13	**+0.06**	+0.07	+0.06	+0.28	+0.16

volume and the real volume of WMH. For a dataset with n observation values, y_1,..., y_n and n corresponding model predictions, f_1, ..., f_n, the coefficient of determination is define as follows:

$$R^2 = 1 - \frac{\sum_i e_i^2}{\sum_i (y_i - \bar{y})^2}, \tag{6.1}$$

where the e_i is the residual $e_i = y_i f_i$. It is used to measure the explanatory

power of the statistical model (Carpenter 1960). The value closer to 1 shows bigger explanatory power. The last row in the Table 6.3 is the regression line of the results which should be $f(x) = 1.0x + 0.0$ ideally.

As shown in the Table 6.3, in terms of various indicators, the third model proposed in this thesis is better than the uResNet and all the other three matured tools.

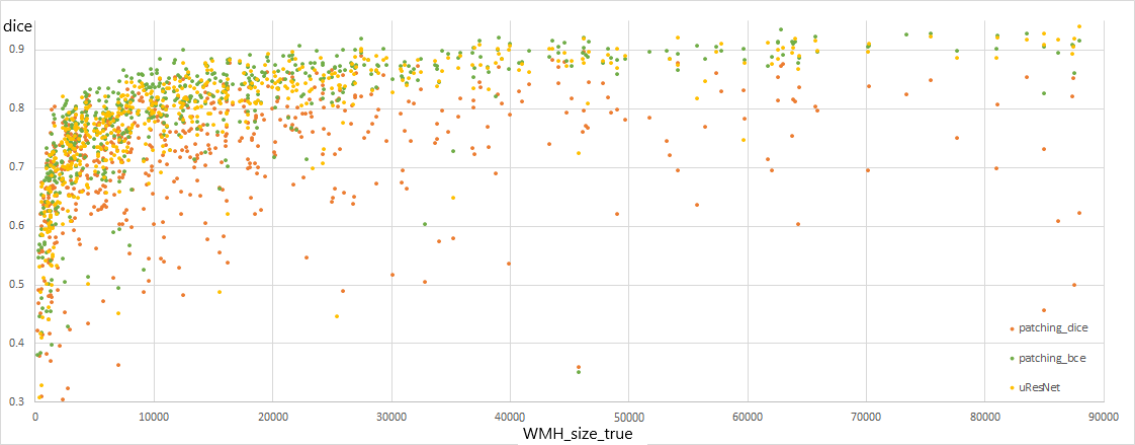

Figure 6.4 *The scatter plot of dices and real WMH volumes.*

Generally, the larger the WMH area is, the easier to segment and the Figure 6.4 proved it. The x axis is the real WMH volume and the y axis is the dice score. Here the result from three method are shown. The yellow dots stand for the result of uResNet (Guerrero et al. 2018). The data is collected from the paper (Nieminen 2018). The green and red dots are the results from patching with binary cross entropy loss and dice loss. The performance of uResNet is between the two models from this thesis. Given these points, The model with both long and short connection with patching and binary cross entropy loss performs best.

6.2 The multi-region segmentation

The first experiment is about the number of the filters in the first and last layer. When we double the filters in the first layer, the number of filters in all the other layers are doubled as well simultaneously. The training time is also doubled at least. In all the U-shaped networks, the number of filters in the first convolutional layer is the same as the number of filters in the last deconvolutional layer. Meanwhile, the expected output is 140 dimensional which indicates that the number of filters in the output layer must be 140. In order to test the design principles mentioned in the paper of Inception V3 (Szegedy et al. 2016),the quantities of the initial filters are set to 16 and 32. The following results were obtained through experiments: the training accuracy increased from 94% to 96% when the filters double and the testing

accuracy raised from 93% to 94%. It is hard to distinguish if the improvement is caused by the principle in Inception V3 (Szegedy et al. 2016) or if more neurons can learn more knowledge.

Another test is about the patching method, from the last section, it is a consensus that patching helps to increase the accuracy. Note that the T1 images for multi-region segmentation is not imbalanced anymore, so the accuracy makes sense. With the non-overlapping patching method in predicting period, a T1 image can be segmented into 27 patches and with overlapping patching method, 80 patches are cut.

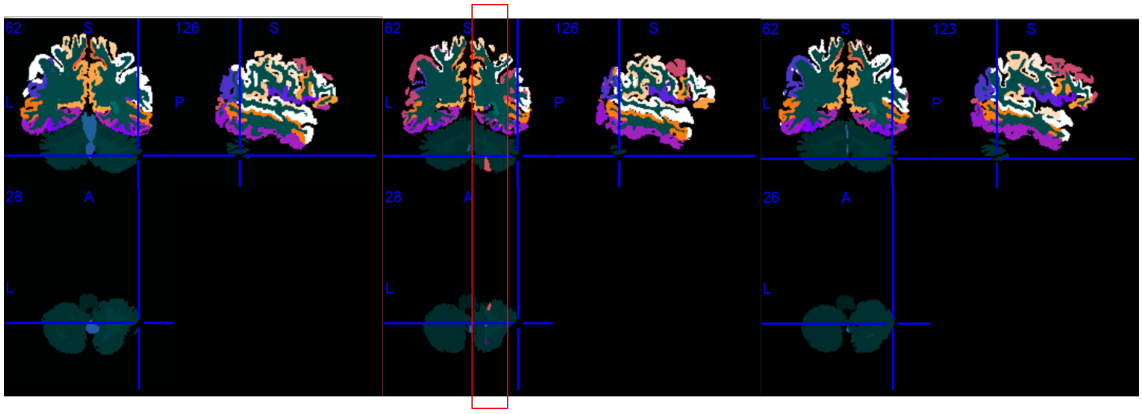

Figure 6.5 *An example of the results using 27 and 80 non-overlapping patches. The left slices are from the corresponding ground truth. The middle slices are from 27 patches and the right slices are from 80 patches.*

Figure 6.5 shows the result from the non-overlapping patching method. Inside the red square there are some errors. The area is not the border of any brain region but the errors seem surrounding a specific vertical line. Obviously, comparing to the Figure 5.9 the line is the edge of patches. When the image is divided into 80 patches so that patches can adjust the result from each other, the errors are disappeared (Figure 6.5, the right slices) .

The final results after 10-fold cross validation of the 1151 T1 images are shown in Figure 6.6 after grouped according to the location. Figure 6.6 shows the dice scores when the brain regions are grouped as listed in Table 4.3. The dice score varies in different brain regions. The bad result about Cerebellar is mainly caused by the segmentation of Cerebellar vermal lobules I-X, especially the Cerebellar vermal lobules I-V whose dice score is just around 0.45. The overall accuracy is above 95%.

If we directly test the network trained from automatic data (1151 T1 images) on manual data (Figure 6.7), the difference between the distributions of two results show the difference between the automatic dataset and the manual dataset (80 manual segmented images).

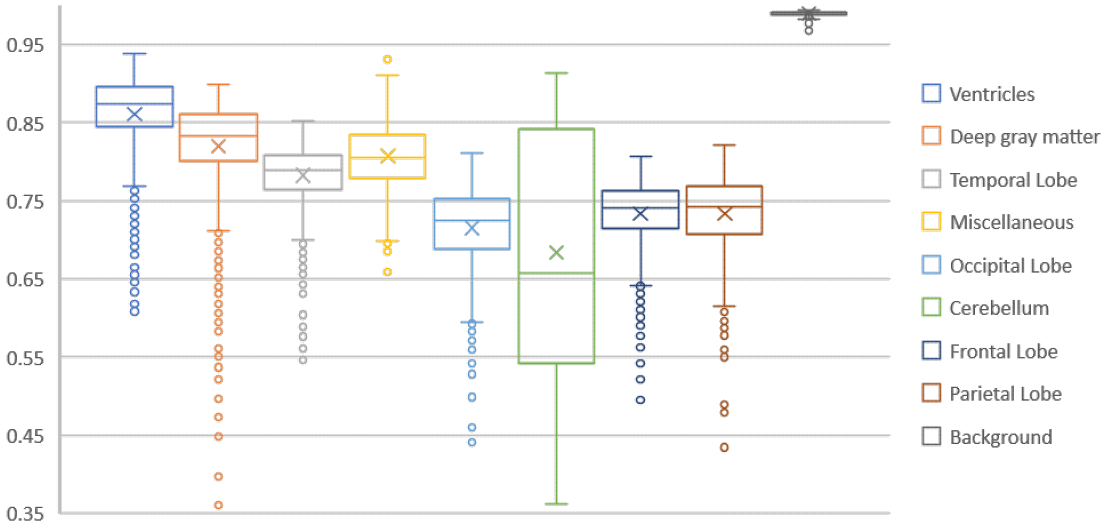

Figure 6.6 *The dice scores in different brain regions. The results are from 1151 T1 images with 32 initial filters and 80 patches for each image.*

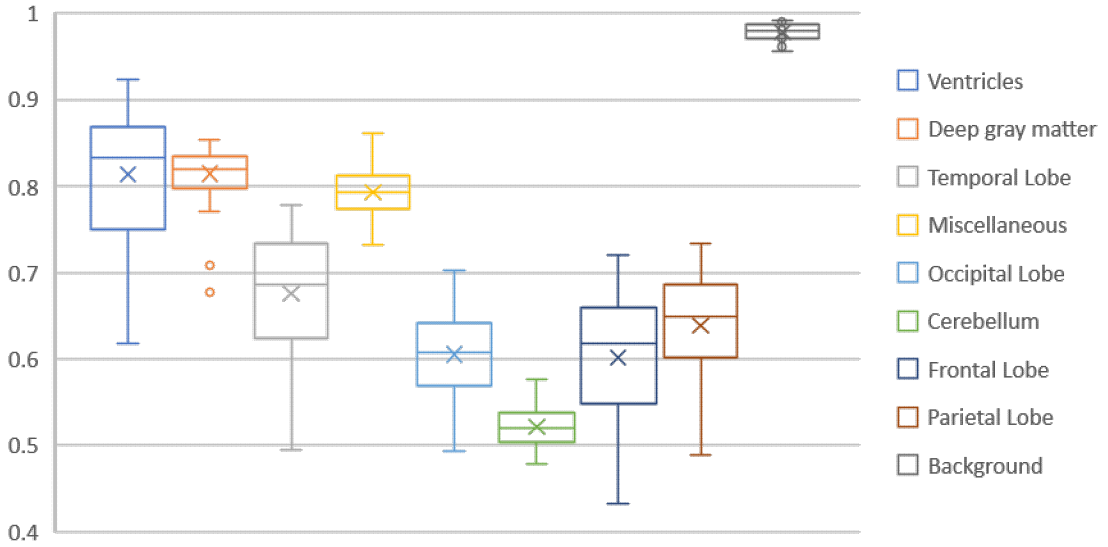

Figure 6.7 *The dice scores in different brain regions. The network is trained using automatic dataset and tested on manual dataset.*

The dice scores in Figure 6.7 are overwhelmingly lower than the corresponding values in the Figure 6.6. First, the result of background is always in a high level, no significant decrease is shown. The overall accuracy goes 2% downward. Consider the brain zones, the result from ventricles, deep gray matter, temporal lobe and miscellaneous drops slightly. On the other hand, a sharp decline happened to the rest four zone (i.e. occipital lobe, cerebellum, frontal lobe and the parietal lobe).

Then a new network is trained with the same architecture but training data is

also manually labeled data. The results after 10-fold cross validation are shown in Figure 6.8.

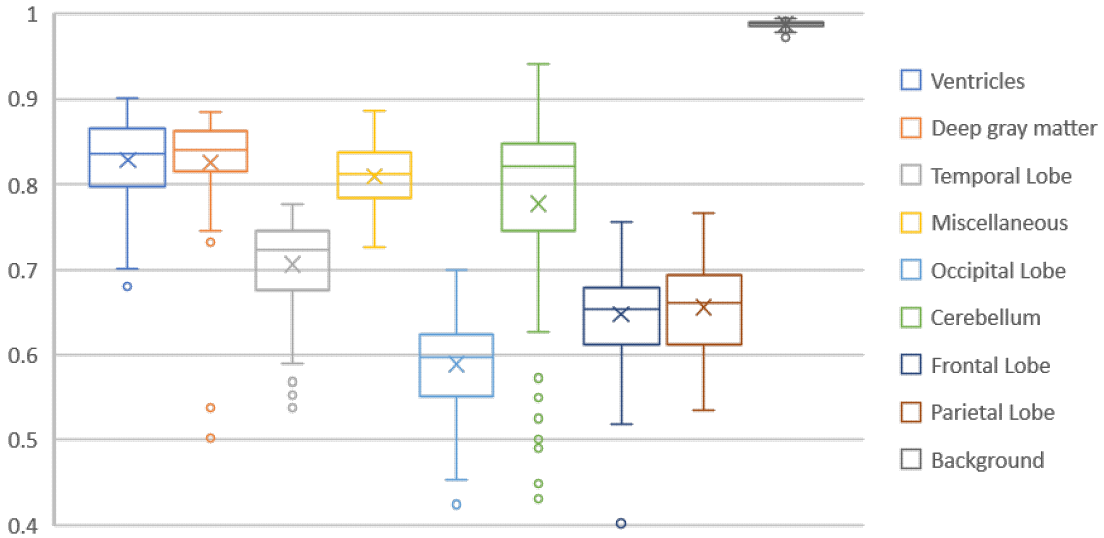

Figure 6.8 *The dice scores in different brain regions for the manual data using cross-validation.*

The accuracy is around 94% when working on the real dataset. Comparing to the result from cross testing (trained using automatic dataset, tested on manual dataset) in Figure 6.7, all the dice scores except the score from occipital lobe improved more or less. The biggest change happened to the cerebellum.

Table 6.4 summarized the dice scores of the automatic dataset and manual dataset via 10-fold cross validation. There are 32 initial neurons in the network and each image is divided into 80 patches.

Table 6.4 *The dice scores of the automatic dataset and manual dataset. The dice scores of the regions that are not appeared in all the images are not shown in this table.*

position	name	automatic	manual
Ventricles	3rd ventricle	0.842	0.827
	4th ventricle	0.809	0.826
	Inferior lateral ventricle	0.747	0.658
	Lateral ventricle	0.940	0.914
Deep gray matter	Accumbens area	0.671	0.686
	Caudate	0.867	0.861
	Pallidum	0.801	0.817
	Putamen	0.870	0.873
	Thalamus proper	0.891	0.889

Temporal Lobe	Amygdala	0.809	0.769
	Hippocampus	0.865	0.860
	Entorhinal area	0.772	0.643
	Fusiform gyrus	0.818	0.711
	Inferior temporal gyrus	0.782	0.662
	Middle temporal gyrus	0.784	0.716
	Parahippocampal gyrus	0.780	0.690
	Planum polare	0.757	0.675
	Planum temporale	0.716	0.623
	Superior temporal gyrus	0.766	0.719
	Temporal pole	0.788	0.741
	Transverse temporal gyrus	0.749	0.667
Miscellaneous	Brain stem	0.931	0.928
	Cerebral exterior	1	1
	Cerebral white matter	0.910	0.841
	CSFnm	0.698	0.770
	Ventral diencephalon	0.862	0.856
	Vessel	0.357	0.404
Occipital Lobe	Calcarine cortex	0.704	0.707
	Cuneus	0.736	0.657
	Inferior occipital gyrus	0.727	0.590
	Lingual gyrus	0.796	0.713
	Middle occipital gyrus	0.722	0.590
	Occipital pole	0.660	0.472
	Occipital fusiform gyrus	0.688	0.472
	Superior occipital gyrus	0.692	0.509
Cerebellum	Cerebellum exterior	0.907	0.903
	Cerebellum white matter	0.891	0.861
	Cerebellar vermal lobules I-V	0.385	0.559
	Cerebellar vermal lobules VI-VII	0.415	0.626
	Cerebellar vermal lobules VIII-X	0.393	0.724
Frontal Lobe	Basal forebrain	0.581	0.426
	Anterior cingulate gyrus	0.792	0.729
	Anterior insula	0.858	0.819
	Anterior orbital gyrus	0.639	0.509
	Central operculum	0.794	0.713
	Frontal operculum	0.733	0.644
	Frontal pole	0.706	0.620

	Gyrus rectus	0.723	0.679
	Lateral orbital gyrus	0.647	0.475
	Middle cingulate gyrus	0.775	0.770
	Medial frontal cortex	0.688	0.571
	Middle frontal gyrus	0.692	0.738
	Medial orbital gyrus	0.777	0.728
	Precentral gyrus medial segment	0.745	0.650
	Superior frontal gyrus medial segment	0.777	0.691
	Opercular part of the inferior frontal gyrus	0.712	0.622
	Orbital part of the inferior frontal gyrus	0.623	0.433
	Posterior orbital gyrus	0.775	0.680
	Precentral gyrus	0.757	0.696
	Subcallosal area	0.743	0.676
	Superior frontal gyrus	0.790	0.736
	Supplementary motor cortex	0.780	0.706
	Triangular part of the inferior frontal gyrus	0.662	0.575
Parietal Lobe	Angular gyrus	0.735	0.606
	Postcentral gyrus medial segment	0.552	0.444
	Posterior cingulate gyrus	0.767	0.735
	Precuneus	0.805	0.738
	Posterior insula	0.833	0.780
	Parietal operculum	0.749	0.656
	Postcentral gyrus	0.713	0.673
	Supramarginal gyrus	0.695	0.609
	Superior parietal Lobule	0.749	0.659

The final study is to train a network with 1151 T1 images and segment two T1 images from one person to test the consistency. Figure 6.9 shows the segmentation results for one patient.

For each pair of T1 images (I_1,I_2) from one patient, a image registration function f(I) is defined so that I_1 can map to I_2 via Equation 6.2.

$$f(I_1) = I_2 \qquad\qquad f^{-1}(I_2) = I_1 \tag{6.2}$$

Subsequently, a dice score of the two results can be calculated in order to measure the similarity of the two segmentations. Here we calculated the dice score of each brain region separately. The same consistency is repeated three times using different segmentation methods. The result is shown in Table 6.5. The values shown are the mean dice scores of the 20 pairs of images. The 'manual' column is the result from

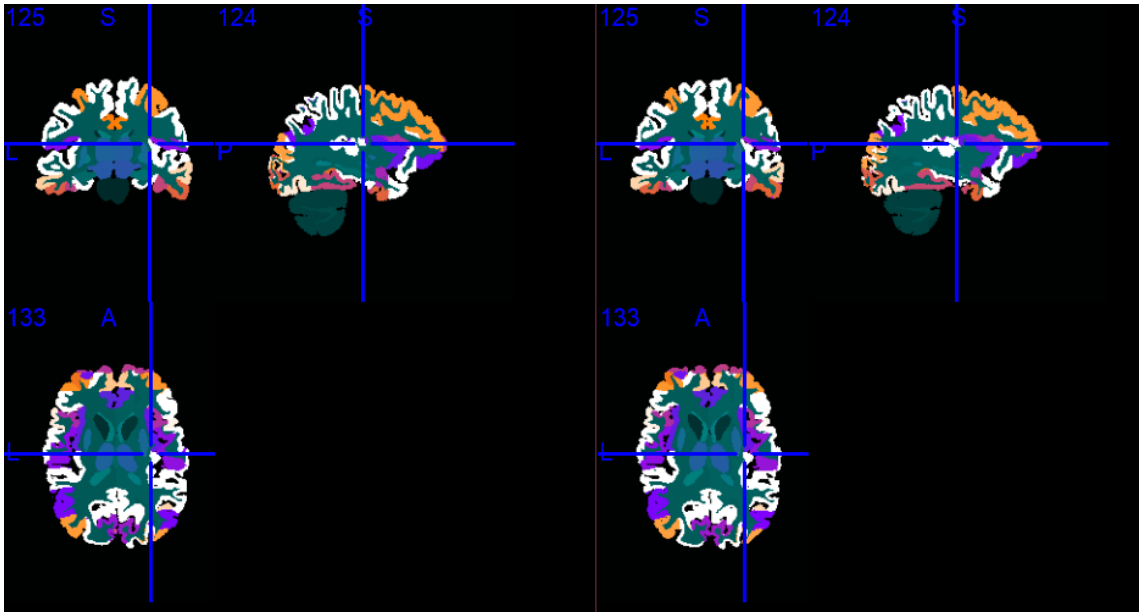

Figure 6.9 *The segmentation result of two T1 images from one patient.*

medical experts. For each pair of images, they are segmented by the same expert. The CNN refers to the 3D U-shaped CNN model proposed in this thesis. The last column shows the results from a mature medical tool named cMRI (Lötjönen, Robin Wolz, Koikkalainen, Thurfjell, et al. 2010) which can do brain image segmentation with atlas based method.

Table 6.5 *The dice scores of the consistency test. The dice scores of the regions that are not appeared in all the 20 pairs of images are not shown in this table.*

position	name	manual	CNN	atlas
Ventricles	3rd ventricle	0.706	0.812	0.875
	4th ventricle	0.817	0.890	0.917
	Inferior lateral ventricle	0.573	0.691	0.804
	Lateral ventricle	0.863	0.925	0.946
Deep gray matter	Accumbens area	0.757	0.868	0.915
	Caudate	0.865	0.932	0.953
	Pallidum	0.832	0.923	0.950
	Putamen	0.873	0.940	0.962
	Thalamus proper	0.902	0.956	0.969
Temporal Lobe	Amygdala	0.784	0.864	0.924
	Hippocampus	0.840	0.925	0.944
	Entorhinal area	0.778	0.805	0.903
	Fusiform gyrus	0.795	0.885	0.913
	Inferior temporal gyrus	0.802	0.850	0.904

	Middle temporal gyrus	0.816	0.877	0.906
	Parahippocampal gyrus	0.753	0.871	0.904
	Planum polare	0.743	0.841	0.886
	Planum temporale	0.701	0.830	0.882
	Superior temporal gyrus	0.797	0.867	0.900
	Temporal pole	0.852	0.897	0.917
	Transverse temporal gyrus	0.727	0.867	0.892
Miscellaneous	Brain stem	0.923	0.958	0.972
	Cerebral exterior	0.918	0.948	0.961
	Cerebral white matter	0.855	0.928	0.952
	CSFnm	0.802	0.860	0.914
	Ventral diencephalon	0.869	0.936	0.953
	Vessel	0.362	0.373	0.715
Occipital Lobe	Calcarine cortex	0.806	0.877	0.905
	Cuneus	0.725	0.830	0.897
	Inferior occipital gyrus	0.763	0.816	0.874
	Lingual gyrus	0.788	0.887	0.911
	Middle occipital gyrus	0.763	0.828	0.869
	Occipital pole	0.769	0.711	0.877
	Occipital fusiform gyrus	0.730	0.815	0.870
	Superior occipital gyrus	0.698	0.782	0.860
Cerebellum	Cerebellum white matter	0.916	0.912	0.960
	Cerebellar vermal lobules I-V		0.690	0.950
	Cerebellar vermal lobules VI-VII		0.157	0.934
	Cerebellar vermal lobules VIII-X		0.173	0.952
Frontal Lobe	Basal forebrain		0.777	0.830
	Anterior cingulate gyrus	0.812	0.897	0.900
	Anterior insula	0.822	0.916	0.932
	Anterior orbital gyrus	0.714	0.826	0.866
	Central operculum	0.777	0.882	0.906
	Frontal operculum	0.725	0.865	0.898
	Frontal pole	0.785	0.811	0.872
	Gyrus rectus	0.760	0.806	0.859
	Lateral orbital gyrus	0.700	0.822	0.866
	Middle cingulate gyrus	0.806	0.899	0.899
	Medial frontal cortex	0.741	0.827	0.860
	Middle frontal gyrus	0.834	0.900	0.916
	Medial orbital gyrus	0.782	0.856	0.896
	Precentral gyrus medial segment	0.760	0.865	0.894

	Superior frontal gyrus medial segment	0.807	0.878	0.896
	Opercular part of the inferior frontal gyrus	0.777	0.867	0.899
	Orbital part of the inferior frontal gyrus	0.699	0.795	0.865
	Posterior orbital gyrus	0.745	0.861	0.902
	Precentral gyrus	0.823	0.872	0.918
	Subcallosal area	0.629	0.792	0.849
	Superior frontal gyrus	0.816	0.887	0.909
	Supplementary motor cortex	0.786	0.886	0.899
	Triangular part of the inferior frontal gyrus	0.765	0.850	0.878
Parietal Lobe	Angular gyrus	0.785	0.840	0.886
	Postcentral gyrus medial segment	0.664	0.698	0.848
	Posterior cingulate gyrus	0.765	0.889	0.902
	Precuneus	0.763	0.871	0.900
	Posterior insula	0.800	0.891	0.915
	Parietal operculum	0.730	0.854	0.887
	Postcentral gyrus	0.794	0.842	0.899
	Supramarginal gyrus	0.785	0.831	0.894
	Superior parietal Lobule	0.784	0.836	0.895

7 Discussion

In this work we proposed a fully covolutional network design, including the hyper-parameter adjustment and a soft-vote based patch-wise post processing method. The combination was tested on 2D and 3D datasets with multiple performance indicators. This method provides a new idea for solving medical image segmentation problems with limited computing power.

Different from the previous networks, after upgrading all neural network layers from 2D to 3D, a residual unit is added to all the convolutional layers. Dropout layers and batch-normalization layers are added to some layers and at the cost of a small increase in computational cost, the time required for convergence is greatly reduced and the accuracy of the prediction is improved. The traditional U-Net keeps discarding the borders of the images during the compressing path which helps to get rid of the influence of the padding. On the other hand, it makes the network constantly change the size of layers to adapt to irregular changes in image size caused by cropped edges. In the network proposed in this thesis, zero-padding is added to each layer, which simplifies the network design. The loss of accuracy caused by zero-padding can be compensated by subsequent soft-voting.

The soft-voting in the ensemble learning area usually refers to combine multiple weakly supervised models to get a better and more comprehensive strong supervised model. In other words, several networks with different architectures are trained and the final result is a weighted average of the outputs from these networks. Together with the accuracy improvement brought by the model-wise soft-voting method, the training time and memory required are also growing linearly. Instead, patch-wise soft-voting proposed in this thesis does not require any extra training cost, but can optimize the performance as well.

As the results in Table 6.3 show the network proposed in this thesis reached higher dice score and lower standard deviation comparing to the uResNet (Guerrero et al. 2018) and some other automatic tools in binary segmentation. In multi-region segmentation, the consistency of our model is better than manual segmentation while the cMRI tool with atlas-based model is still better. The biggest advantage of the machine learning model comparing to the traditional atlas based model is the high efficiency. The cMRI tool takes around 20 minutes to do multi-region segmentation on an image while the neural network takes only 1-2 minutes.

By comparing Figure 6.6 and Figure 6.7, it is clearly shown that the model generalized from automatic dataset is unfit to the manual dataset. The reason might be the man-made mistakes when labeled by human, different weight should be chosen to manual data and automatic data or the imperfection of the atlas-based

model used to create the 1151 images.

In the diagnostics of the AD, not all the regions in the brain are equally important. Hippocampus is one of the most important region. The ultimate goal of the automatic segmentations is to achieve the accuracy of two manual segmentations. Table 7.1 shows the consistency results of two manual segmentations of hippocampus from other studies. It shows that there are unavoidable errors even in manual segmentations. Therefore, when we usually use the manual segmentation as the ground truth, the perfect match cannot be expected. The final aim is not to train a neural network which is able to segment images exactly the same as human, but to let the consistency of the automatic segmentation at the same level as the manual segmentation. Because if there is perfect match, then if we take another manual segmentation as the ground truth, there will be some differences. The results show that the consistency of the CNN model in this thesis is not inferior to some manual segmentations. In this thesis, the consistency result from the neural network is higher than from the two manual segmentations.

Table 7.1 *The results for the inter-rater variability of the manual segmentation as well as the automatic segmentation proposed in this thesis of hippocampus. N stands for the number of sample image pairs. The last column is the correlation coefficient between the volumes of two manual segmentations.*

HIPPOCAMPUS from MRI	**dice score**	**correlation coefficient**
Morra et al. 2009, NeuroImage (N=21)	0.85	0.71
Lijn et al. 2008, NeuroImage (N=20)	0.86	0.83
Niemann et al. 2000, Psych. Res (N=20)	-	0.93
Leung et al. 2010, NeuroImage (N=15)	0.93	0.95
This thesis, two CNN segs(N=20)	0.93	0.96
This thesis, two manual segs(N=20)	0.84	0.87

In the future, the network together with the atlas-based segmentation method which is used to produce training data for multi-region segmentation task can form the prototype of a generative adversarial network (Goodfellow et al. 2014). The neural network model and atlas-based model can be iteratively optimized in the future work. This means that atlas-based model is used to generate data and the neural network is used to evaluate the data quality. Besides that, attention units (F. Wang et al. 2017) and model-wise patching method can be added to the network as well.

Moreover, there are some limitations in this network, for instance, the catastrophic forgetting (French 1999). After learning new information, the network almost completely forgot what it learned before. Unluckily, it happened to the multi-region segmentation. For instance, with a training dataset containing 1000 T1 images, we could generate $1000 \times 100 = 10^5$ patches to train the network. But

in practise, there is no significant difference between training the network with 10^3 patches or 10^5 patches after 50 epochs except the training time. It shows that in the training period the number of patches that the network can remember does not exceed 1000. There are also some data-related limitations. The slice thickness of the original FLAIR image is $5 - 7.5mm^3$ which is too thick. The ideal thickness should be $1mm^3$. Besides that, the size of manual segmentation dataset should be increased.

8 Conclusion

This research work has proposed a deep-learning based brain MRI segmentation architecture. Several tests were designed. First, the contrast of the result from 2D sequential images and 3D images was shown. Then the experiments presents how the depth, width and the weight distribution in layers of a neural network influence the performance. Third, we discussed the importance of data balance and balanced the data by resizing and patching. Finally, a soft-vote based patch-wise post-processing is proved effective.

The final result shows that the designed network can do both binary segmentation and multi-region segmentation precisely. The dice score reached 0.783 in binary segmentation and accuracy reached 96% in multi-region segmentation. The network also passed the consistency test with high score. By comparing to some atlas-based models, the CNN based models could be an alternative choice in the medical segmentation area in the near future.

The segmentation algorithm proposed in this paper has great value in clinical and scientific research fields. It provides a fast and accurate method to quantify medical imaging data, for example, for diagnostics, treatment planning, and follow-up of disease progression. The multi-region MRI segmentation can be generalized to the multi-class semantic segmentation of complex images in real life. It also has great development potential in the field of image information collection.

References

Avants, Brian B, Nick Tustison, and Gang Song (2009). "Advanced normalization tools (ANTS)". In: *Insight Journal* 2.365, pp. 1–35.

Bevington, J and R Mersereau (1987). "Differential operator based edge and line detection". In: *ICASSP'87. IEEE International Conference on Acoustics, Speech, and Signal Processing*. Vol. 12. IEEE, pp. 249–252.

Bishop, Christopher M et al. (1995). *Neural networks for pattern recognition*. Oxford University Press, p. 198.

Bouvrie, Jake (2006). *Notes on convolutional neural networks*. English. URL: `http://cogprints.org/5869/1/cnn_tutorial.pdf`.

Carpenter, RG (1960). "Principles and procedures of statistics, with special reference to the biological sciences". In: *The Eugenics Review* 52.3, p. 172.

Carreira, Joao et al. (2012). "Semantic segmentation with second-order pooling". In: *European Conference on Computer Vision*. Springer, pp. 430–443.

Chang, Yian-Leng and Xiaobo Li (1994). "Adaptive image region-growing". In: *IEEE transactions on image processing* 3.6, pp. 868–872.

Çiçek, Özgün et al. (2016). "3D U-Net: learning dense volumetric segmentation from sparse annotation". In: *International Conference on Medical Image Computing and Computer-assisted Intervention*. Springer, pp. 424–432.

Cocosco, Chris A et al. (1997). "Brainweb: Online interface to a 3D MRI simulated brain database". In: *NeuroImage*. Citeseer. URL: `http://citeseerx.ist.psu.edu/viewdoc/summary?doi=10.1.1.51.3917`.

Cybenko, George (1989). "Approximation by superpositions of a sigmoidal function". In: *Mathematics of Control, Signals and Systems* 2.4, pp. 303–314.

Dibal, PY et al. (2018). "Enhanced discrete wavelet packet sub-band frequency edge detection using Hilbert transform". In: *International Journal of Wavelets, Multiresolution and Information Processing* 16.01, p. 1850009.

Drozdzal, Michal et al. (2016). "The importance of skip connections in biomedical image segmentation". In: *Deep Learning and Data Labeling for Medical Applications*. Springer, pp. 179–187.

Duchi, John, Elad Hazan, and Yoram Singer (2011). "Adaptive subgradient methods for online learning and stochastic optimization". In: *Journal of Machine Learning Research* 12.Jul, pp. 2121–2159.

Dumoulin, Vincent and Francesco Visin (2016). "A guide to convolution arithmetic for deep learning". In: *arXiv preprint arXiv:1603.07285*.

Duvenaud, David et al. (2014). "Avoiding pathologies in very deep networks". In: *Artificial Intelligence and Statistics*, pp. 202–210.

French, Robert M (1999). “Catastrophic forgetting in connectionist networks”. In: *Encyclopedia of Cognitive Science* 3.4, pp. 128–135.

Goodfellow, Ian et al. (2014). “Generative adversarial nets”. In: *Advances in neural information processing systems*, pp. 2672–2680.

Guerrero, R et al. (2018). “White matter hyperintensity and stroke lesion segmentation and differentiation using convolutional neural networks”. In: *NeuroImage: Clinical* 17, pp. 918–934.

He, Kaiming et al. (2015). “Delving deep into rectifiers: Surpassing human-level performance on imagenet classification”. In: *Proceedings of the IEEE International Conference on Computer Vision*, pp. 1026–1034.

— (2016). “Deep residual learning for image recognition”. In: *Proceedings of the IEEE Conference on Computer Vision and Pattern Recognition*, pp. 770–778.

Hochreiter, Sepp et al. (2001). *Gradient flow in recurrent nets: the difficulty of learning long-term dependencies*.

Ioffe, Sergey and Christian Szegedy (2015). “Batch normalization: Accelerating deep network training by reducing internal covariate shift”. In: *arXiv preprint arXiv: 1502.03167*.

Kamnitsas, Konstantinos, Wenjia Bai, et al. (2017). “Ensembles of multiple models and architectures for robust brain tumour segmentation”. In: *International MICCAI Brainlesion Workshop*. Springer, pp. 450–462.

Kamnitsas, Konstantinos, Christian Ledig, et al. (2017). “Efficient multi-scale 3D CNN with fully connected CRF for accurate brain lesion segmentation”. In: *Medical Image Analysis* 36, pp. 61–78.

Kingma, Diederik P and Jimmy Ba (2014). “Adam: A method for stochastic optimization”. In: *arXiv preprint arXiv:1412.6980*.

Kolomenkin, Michael, Ilan Shimshoni, and Ayellet Tal (2009). “On edge detection on surfaces”. In: *2009 IEEE Conference on Computer Vision and Pattern Recognition*. IEEE, pp. 2767–2774.

Krizhevsky, Alex, Ilya Sutskever, and Geoffrey E Hinton (2012). “Imagenet classification with deep convolutional neural networks”. In: *Advances in neural information processing systems*, pp. 1097–1105.

Kurita, Takio, Nobuyuki Otsu, and N Abdelmalek (1992). “Maximum likelihood thresholding based on population mixture models”. In: *Pattern Recognition* 25.10, pp. 1231–1240.

Leung, Kelvin K et al. (2010). “Automated cross-sectional and longitudinal hippocampal volume measurement in mild cognitive impairment and Alzheimer’s disease”. In: *Neuroimage* 51.4, pp. 1345–1359.

Li, Jun (2003). "A wavelet approach to edge detection". PhD thesis. Sam Houston State University. URL: http://citeseerx.ist.psu.edu/viewdoc/download?doi=10.1.1.89.4443&rep=rep1&type=pdf.

Lijn, Fedde van der et al. (2008). "Hippocampus segmentation in MR images using atlas registration, voxel classification, and graph cuts". In: *Neuroimage* 43.4, pp. 708–720.

Lin, Min, Qiang Chen, and Shuicheng Yan (2013). "Network in network". In: *arXiv preprint arXiv:1312.4400*.

Lin, Tsung-Yi et al. (2017). "Focal loss for dense object detection". In: *Proceedings of the IEEE International Conference on Computer Vision*, pp. 2980–2988.

Long, Jonathan, Evan Shelhamer, and Trevor Darrell (2015). "Fully convolutional networks for semantic segmentation". In: *Proceedings of the IEEE Conference on Computer Vision and Pattern Recognition*, pp. 3431–3440.

Lötjönen, Jyrki, Robin Wolz, Juha Koikkalainen, Valtteri Julkunen, et al. (2011). "Fast and robust extraction of hippocampus from MR images for diagnostics of Alzheimer's disease". In: *Neuroimage* 56.1, pp. 185–196.

Lötjönen, Jyrki, Robin Wolz, Juha Koikkalainen, Lennart Thurfjell, et al. (2010). "Fast and robust multi-atlas segmentation of brain magnetic resonance images". In: *Neuroimage* 49.3, pp. 2352–2365.

McRobbie, Donald W et al. (2017). *MRI from Picture to Proton*. Cambridge University Press.

Milletari, Fausto, Nassir Navab, and Seyed-Ahmad Ahmadi (2016). "V-net: Fully convolutional neural networks for volumetric medical image segmentation". In: *2016 Fourth International Conference on 3D Vision (3DV)*. IEEE, pp. 565–571.

Monga, Olivier and Serge Benayoun (1995). "Using partial derivatives of 3D images to extract typical surface features". In: *Computer Vision and Image Understanding* 61.2, pp. 171–189.

Morra, Jonathan H et al. (2009). "Automated mapping of hippocampal atrophy in 1-year repeat MRI data from 490 subjects with Alzheimer's disease, mild cognitive impairment, and elderly controls". In: *Neuroimage* 45.1, S3–S15.

Niemann, Klaus et al. (2000). "Evidence of a smaller left hippocampus and left temporal horn in both patients with first episode schizophrenia and normal control subjects". In: *Psychiatry Research: Neuroimaging* 99.2, pp. 93–110.

Nieminen, Tuomas J. (2018). "Deep learning in quantifying vascular burden from brain images". MA thesis. Tampere University. URL: http://urn.fi/URN:NBN:fi:tty-201804261565.

Nomura, Atsushi et al. (2011). "Edge detection algorithm inspired by pattern formation processes of reaction-diffusion systems". In: *International Journal of Circuits, Systems and Signal Processing* 5.2, pp. 105–115.

Parvati, K, Prakasa Rao, and M Mariya Das (2008). "Image segmentation using gray-scale morphology and marker-controlled watershed transformation". In: *Discrete Dynamics in Nature and Society* 2008, Article ID 384346.

Radford, Alec, Luke Metz, and Soumith Chintala (2015). "Unsupervised representation learning with deep convolutional generative adversarial networks". In: *arXiv preprint arXiv:1511.06434*.

Ronneberger, Olaf, Philipp Fischer, and Thomas Brox (2015). "U-net: Convolutional networks for biomedical image segmentation". In: *International Conference on Medical Image Computing and Computer-assisted Intervention*. Springer, pp. 234–241.

Schmidt, Paul (2017). "Bayesian inference for structured additive regression models for large-scale problems with applications to medical imaging". PhD thesis. Ludwig Maximilian University.

Schmidt, Paul et al. (2012). "An automated tool for detection of FLAIR-hyperintense white-matter lesions in multiple sclerosis". In: *Neuroimage* 59.4, pp. 3774–3783.

Seiler, Mary C and Fritz A Seiler (1989). "Numerical recipes in C: the art of scientific computing". In: *Risk Analysis* 9.3, pp. 415–416.

Sharma, Neeraj and Lalit M Aggarwal (2010). "Automated medical image segmentation techniques". In: *Journal of Medical Physics/Association of Medical Physicists of India* 35.1, p. 3.

Shenton, Martha E et al. (2001). "A review of MRI findings in schizophrenia". In: *Schizophrenia Research* 49.1-2, pp. 1–52.

Simonyan, Karen and Andrew Zisserman (2014). "Very deep convolutional networks for large-scale image recognition". In: *arXiv preprint arXiv:1409.1556*.

Srivastava, Nitish et al. (2014). "Dropout: a simple way to prevent neural networks from overfitting". In: *The Journal of Machine Learning Research* 15.1, pp. 1929–1958.

Szegedy, Christian et al. (2016). "Rethinking the inception architecture for computer vision". In: *Proceedings of the IEEE Conference on Computer Vision and Pattern Recognition*, pp. 2818–2826.

Tieleman, Tijmen and Geoffrey Hinton (2012). "Lecture 6.5-rmsprop: Divide the gradient by a running average of its recent magnitude". In: *COURSERA: Neural networks for machine learning* 4.2, pp. 26–31.

Turchenko, Volodymyr, Eric Chalmers, and Artur Luczak (2017). "A deep convolutional auto-encoder with pooling-unpooling layers in caffe". In: *arXiv preprint arXiv:1701.04949*.

Vandenberghe, Stefaan and Paul K Marsden (2015). "PET-MRI: a review of challenges and solutions in the development of integrated multimodality imaging". In: *Physics in Medicine & Biology* 60.4, R115.

Waldemar, G (2002). “Age-related white matter changes as a predictor of disability in the elderly: the LADIS (Leukoaraiosis and DISability) project”. In: *European Journal of Neurology* 9.suppl 2, p. 41.

Wang, Fei et al. (2017). “Residual attention network for image classification”. In: *Proceedings of the IEEE Conference on Computer Vision and Pattern Recognition*, pp. 3156–3164.

Wang, Haishen et al. (2013). “Soft-voting clustering ensemble”. In: *International Workshop on Multiple Classifier Systems*. Springer, pp. 307–318.

Werbos, Paul (1974). “Beyond regression:” new tools for prediction and analysis in the behavioral sciences”. In: *Ph. D. dissertation, Harvard University*.

Wu, Qing and Yizhou Yu (2004). “Feature matching and deformation for texture synthesis”. In: *ACM Transactions on Graphics (TOG)* 23.3, pp. 364–367.

Xie, Saining and Zhuowen Tu (2015). “Holistically-nested edge detection”. In: *Proceedings of the IEEE International Conference on Computer Vision*, pp. 1395–1403.

Yan, Zhennan et al. (2017). “Multi-instance multi-stage deep learning for medical image recognition”. In: *Deep Learning for Medical Image Analysis*. Elsevier, pp. 83–104.

APPENDIX

1 Glossary

2D two-dimensional. 1

3D three-dimensional. 1

ANN artificial neural network. 8

BCE binary cross entropy. 42

CNN convolutional neural network. 13

CSF cerebrospinal fluid. 28, 49, 52

CV cross validation. 42

FCN fully convolutional network. 5

FN false negative. 12

FP false positive. 12

GPU Graphics Processing Unit. 31

GT ground truth. 27

ICV Total Intracranial Volume. 42

IDE Integrated Development Environment. 40

ILSVRC ImageNet Large Scale Visual Recognition Challenge. 4

LADIS eukoaraiosis And DISability. 24

LPA The lesion prediction algorithm. 44

MRI magnetic resonance imaging. 1

PDP parallel decentralized processors. 8

PReLU Parametric Rectified Linear Unit. 22

ReLU Rectified Linear Unit. 10

ResNet residual network. 4

RGB red, green, blue. 2

T2 T2-weighted image. 24

TP true positive. 12

VGGNet Very Deep Convolutional Network. 1